

University of Groningen

**Prospects of PbS NCs in hybrid solar cells
and the effects of ligand exchange
on NC properties**

Mark Jonathan Speirs

Prof. Dr. M.A. Loi

Dr. K. Szendrei

January 2012



**university of
 groningen**

**faculty of mathematics
 and natural sciences**

Thesis submitted by:

Mark Jonathan Speirs

Student number: s1626124

As required for the completion of:

Msc. Applied Physics,

Faculty of Mathematics and Natural Sciences,

University of Groningen

The research for this thesis was done in the group:

Photophysics and OptoElectronics

Led by:

Prof. Dr. Maria Antonietta Loi

Supervised by:

Dr. Krisztina Szendrei

Abstract

LEAD SULFIDE NANOCRYSTALS form an interesting prospective semiconductor for photovoltaic applications, offering the possibility of a low-cost, physically flexible material with the advantage of a highly tunable material band gap via the quantum confinement effect. In this study we explore the use of PbS nanocrystals as active material in hybrid NC-organic device structures. First, Schottky devices of PbS NCs achieving excellent efficiencies of up to 4.0% are demonstrated. High fill factors of up to 59% are realized in bilayer devices consisting of PbS NCs and PCBM indicating highly efficient exciton dissociation at the type-II heterojunction. Devices incorporating a bulk-heterojunction of PbS and PCBM are fabricated, yielding an improved efficiency of 3.1% compared to a 2.9% efficiency of a referential Schottky device. TEM images of NC films made before and after ligand exchange show that inter-particle spacing is decreased from ~ 2 nm for NCs capped with long oleic acid ligands to ~ 0.5 nm after treatment with crosslinking 1,4-BDT molecules. This induces irregular NC spacing, due to non-homogeneous crosslinking of the individual NCs, and facilitates wave function overlap of electrons in adjacent crystals, greatly improving film conductivity. Temperature dependent PL measurements are performed before and after BDT treatment. Heavy temperature dependence of the PL spectra is observed in both cases. For NCs capped with oleic acid ligands a decrease in temperature results in a redshift of the PL peaks together with an increase of the signal intensity. After treatment with BDT the PbS films exhibit unusual properties such as irregular shape of the spectra and a decrease of the PL signal, which could be attributed to the increased probability of nonradiative recombination at lower temperatures.

Acknowledgements

First and foremost, I would like to express my gratitude to Prof. Maria Antonietta Loi for giving me the opportunity to do my master research project in her group, as well as giving me guidance, advice, and useful directions during this time. I also owe a huge Thank You to my supervisor Krisztina Szendrei for all her ideas, help, and encouragement, and for making my research an enjoyable experience! To the staff members Jan Harkema and Frans van der Horst I would like to express my appreciation for all their troubleshooting and provision in the lab. Furthermore, I would like to thank Widi for showing me the ropes in the cleanroom, Dorota for the expertise and time she gave with the spectroscopy measurements, Paul de Bruyn for sharing some good ideas, and Prof. Bart Kooi for his assistance in creating some beautiful TEM images. I would also like to thank Alex and Martijn for their help in the cleanroom and finally, a thank you to all the other members of the group for their fun company, and for being patient when I endlessly occupied the glovebox whilst processing my samples.

Contents

1	Introduction	1
2	Theory	5
2.1	Concepts of inorganic solar cells	5
2.2	Concepts of organic solar cells	7
2.3	Device parameter characterization	9
2.4	Schottky junction devices	12
2.5	Hybrid solar cell devices	13
2.5.1	Bilayer heterojunction solar cells	14
2.5.2	Bulk-heterojunction solar cells	15
2.6	Nanocrystals as PV material	16
3	Methods	19
3.1	Materials	19
3.1.1	Glass and ITO	19
3.1.2	PbS nanocrystals	20
3.1.3	1,4-Benzenedithiol	20
3.1.4	[6,6]-phenyl-C61-butyric acid methyl ester	20
3.1.5	Poly(3-hexylthiophene)	21
3.1.6	PCPDTBT	21
3.1.7	Aluminium and lithium fluoride	22
3.1.8	Solvents	22
3.2	Device fabrication	23
3.2.1	Fabrication steps	23
3.2.2	Device recipes	26
3.3	Measurement techniques	29
3.3.1	J-V characteristics	29
3.3.2	IPCE measurements	30
3.3.3	Thickness measurements	31

3.3.4	TEM imaging	31
3.3.5	Spectroscopy measurements	32
4	Results	33
4.1	Schottky device	33
4.2	Bilayer device	36
4.3	Bulk-heterojunction device	38
4.4	TEM measurements	40
4.5	Optical properties of PbS NCs	40
5	Conclusions	44
	References	46

Introduction

In recent times, we have seen the concentration of greenhouse gases in the earth's atmosphere rise significantly due to the rapid burning of carbon based fossil fuels as a source of energy on a global scale. If unchecked, this increase in greenhouse gasses may lead to an increase in the temperature of earth's oceans and lower atmosphere. It is believed that such an increase in temperature will have several negative effects on our environment, such as melting of land ice causing rising sea levels; increasing fluctuations of climate extremes; increased desertification; and loss of agricultural land. For this reason, and because the global supply of fossil fuel is limited, a strong interest has emerged for the development of clean and renewable sources of energy such as wind, solar and hydroelectric power.

Solar power in particular is a promising source of energy due to the abundance of energy that reaches the earth's surface from the sun. To illustrate this point, annual global energy consumption is in the order of $\sim 4 \cdot 10^{20} J$ whereas the annual global insolation is $\sim 3 \cdot 10^{24} J$, an excess of more than three orders of magnitude.[1, 2] Photovoltaic (PV) energy conversion is a particularly attractive method of harvesting solar power, as it produces zero emissions and noise while in operation, requires low maintenance and is visually unobtrusive. Photovoltaic cells are made from semiconducting materials and are based on the photoelectric effect described by Einstein. This mechanism describes the excitation of charge carriers to a higher state of energy upon absorption of a photon.[3] Under appropriate conditions the excitation energy can be harvested and converted into electrical current.

So far the PV market has been dominated by cells made of highly purified silicon crystals. Power conversion efficiencies (PCE's) as high as 25% under standard testing conditions have been reached for monocrystalline silicon wafers, while the first generation of commercial solar cells exhibit PCEs of 16-18%.[4] Despite these relatively high efficiencies, there are significant drawbacks to the large-scale production of silicon-based

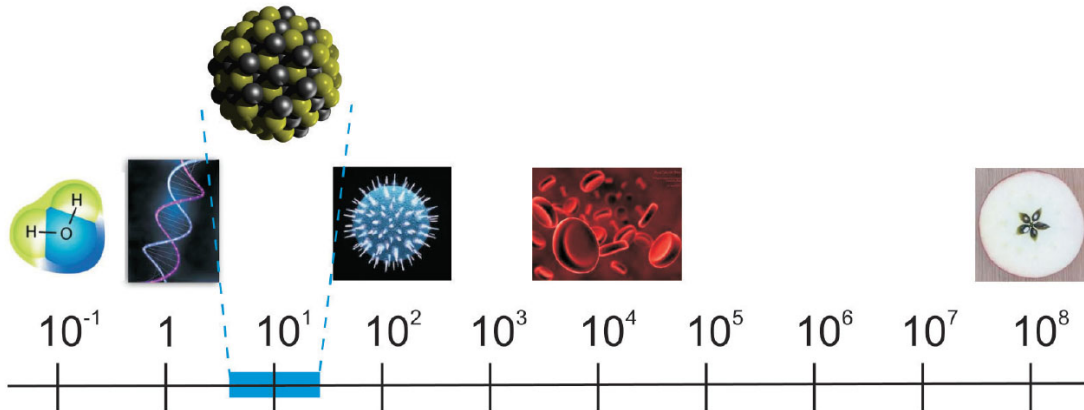


Figure 1.1: Dimension comparison of NCs in nanometers.

PV devices. Monocrystalline silicon wafers require a large amount of energy to produce, are inherently fragile and require a complicated production process including several etching steps, resulting in a long payback time, both economically and energetically. Organic, or ‘plastic’, solar cells have therefore attracted interest, featuring significantly lower production costs. They are often made from conjugated polymers, which exhibit semiconducting properties, allowing them to be used in PV applications while maintaining many of the beneficial properties exhibited by plastics. They are easy to produce, lightweight and flexible. This allows them to be used in many applications where the rigid and fragile silicon based PV cells can not. Furthermore, conjugated polymers generally have a high absorption coefficient, requiring only a thin layer to absorb most of the incident light, so very little material is required. In addition, these materials are generally soluble in organic solvents, allowing for low cost production techniques such as roll-to-roll printing and spin coating. Notwithstanding these advantages, organic photovoltaic (OPV) cells come with two considerable disadvantages. The most significant is their comparatively low efficiencies, with highest reported values of 3.5% for single layer organic devices and 8.3% for tandem organic solar cells.[4] The second major disadvantage of OPV cells is their short lifespan in air. The efficiency of organic devices decays rapidly due to chemical reactions with water and especially oxygen. Increasing device stability is therefore one of the challenges that will have to be met if OPV solar cells are to form a significant source of energy in the future.

OPV efficiencies are limited in large part by the low mobility of charge carriers through the material and inefficient charge separation of electron-hole pairs. This can be improved by combining organic materials with a suitable inorganic material. Inorganic nanocrystal (NC) materials such as PbS, PbSe, and CdTe have been shown to be very promising in this respect, providing high absorption and mobility. In addition, NCs have very interesting properties due to their size which is in the order of several nanometers,

see Figure 1.1. In this size regime, the material band gap is largely determined by the quantum confinement effect and can therefore be tuned by their size to facilitate charge separation and harvest parts of the solar spectrum that would otherwise go unused, such as the infrared region. Semiconducting nanocrystals have been reported to harvest wavelengths extending far beyond the visible, even up to $2\ \mu\text{m}$. [5, 6]

Besides size, NC characteristics are strongly influenced by surface properties. NCs are capped with a shell of ligands providing solubility and preventing aggregation but also hindering charge extraction. These ligands must be replaced by shorter, more conductive molecules to facilitate charge transport and achieve improved device performance. Such ligand exchange results in a much decreased particle spacing as can be seen in Figure 1.2. However, the consequences hereof with regard to the electrical and optical properties of the NCs are only partially understood, even though they play a significant role in determining device efficiency. Thus, one of the goals of this study is to investigate the physics behind the different ligands and their effect on device performance.

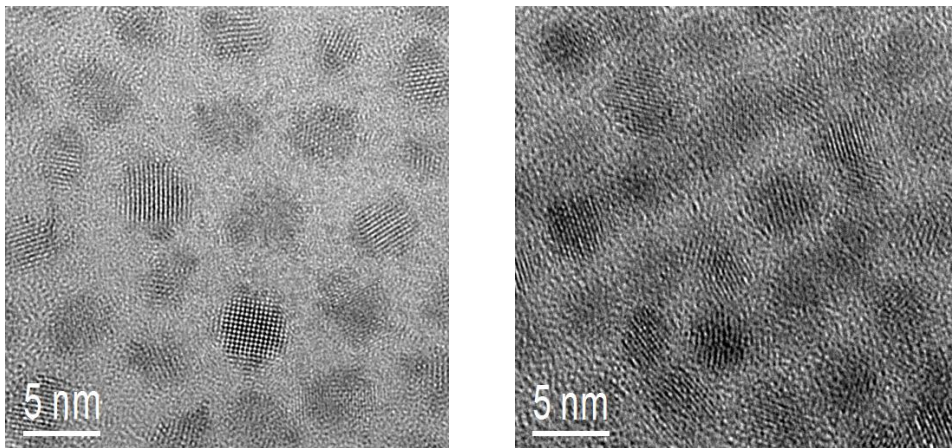


Figure 1.2: PbS NCs (a) before and (b) after exposure to 1,4-BDT

In inorganic semiconductors, photoexcited charge carriers can move freely through the conduction and valence band. Organic semiconductors however, form tightly bound excitons upon photon absorption. An efficient method of exciton dissociation can take place at an interface of two materials of different energy levels. However, exciton diffusion lengths are typically only around 20 nm so that only excitons formed near a heterojunction interface contribute to the photocurrent.[7] It is therefore beneficial to have a heterojunction interface within the exciton diffusion length at every point in the material, a so called bulk-heterojunction. Hybrid nanocrystal-organic PV structures show great potential in effectively solving this problem and forming efficient, yet easily processable PV devices. This study explores the usage of lead sulfide (PbS) in hybrid NC-inorganic solar cells.

In Chapter 2 the theory of different PV devices will be treated. The experimental methods will be addressed in Chapter 3, and the results thereof will be presented and discussed in Chapter 4. Finally, conclusions will be presented in Chapter 5.

Theory

In order to improve solar cell efficiencies in inorganic-organic hybrid solar cell structures, it is essential to understand the mechanisms that drive inorganic and organic solar cells. The concepts underlying inorganic solar cells will therefore be discussed first, followed by those of organic solar cells and the difference between the two. Next, the parameters that characterize a solar cell will be discussed. Thereafter, a description of the various device structures investigated in this study will be presented: Schottky devices, bilayer devices and bulk heterojunction devices. Finally, inorganic PbS NCs and their effect on device parameters will be discussed.

2.1 Concepts of inorganic solar cells

Inorganic solar cells generally consist of both an n-type semiconductor material with an excess of negative charge carriers (electrons), and a p-type semiconductor with an excess of positive charge carriers (holes). This combination is referred to as a p-n junction. When put in intimate contact with each other, the energy levels of the n- and p- materi-

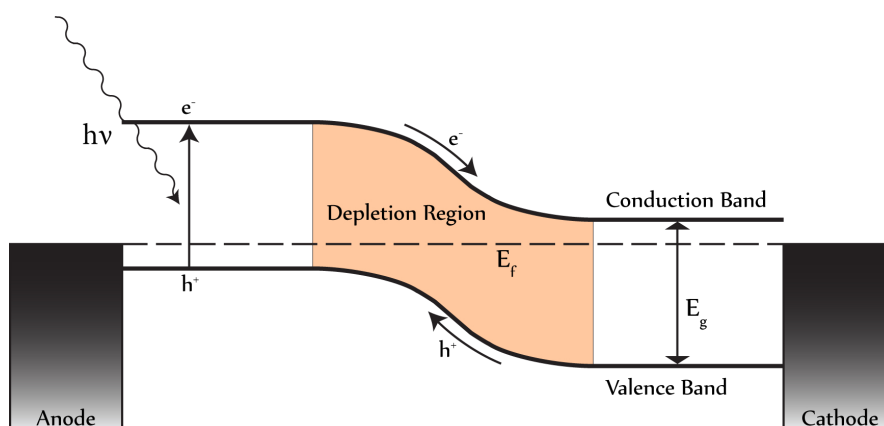


Figure 2.1: Band energy diagram of an inorganic p-n solar cell

als bend in such a way that their Fermi levels align, as required by thermal equilibrium. At the interface of the p-n junction, electrons diffuse from the n-type side where the free electron density is high to the p-type side where the electron density is low. Here they recombine with the holes of the p-type material. The reverse occurs for the positive charge carriers, holes from the p-side diffuse to the n-side and recombine with the electrons in the n-type material. This creates a region near the interface where there are very few mobile charge carriers, called the depletion region or space charge region, see Figure 2.1. Due to this diffusion, charge builds up on both sides of the interface and creates a built-in electric field which opposes the diffusion. The diffusion stops when the electric force exactly cancels out the diffusion force.

Particularly interesting for our purposes is the p-n junction's response to an incident light source. Light emitted from the sun (or any source) comes in quantized packages called photons. Photons have energy equal to $h\nu$, or equivalently hc/λ , where ν and λ are the light's frequency and wavelength respectively, h is Planck's constant and c is the speed of light. A photon incident on a semiconductor may be absorbed, reflected or transmitted. For a photon to be absorbed it must have energy larger than the band gap E_g of the material, which is the difference between the highest energy state of the valence band and the lowest energy state of the conduction band. For example, silicon, the most prolific PV material used to date, has a well-established band gap of 1.1 eV. Before excitation, the electron is tightly bound in a covalent bond between neighboring atoms in the crystal lattice of the semiconductor. When a photon is absorbed a free electron-hole pair is created by excitation of an electron from this tightly bound state in the valence band to the conduction band, where it is free to travel throughout the material. The excited electron leaves behind a mobile hole in the valence band. This can occur both in the bulk of the material or in the depletion region. The photon energy must be larger than the band gap because the electrons are part of an energetically favorable covalent bond, which must be broken before the transition of the electron to the conduction band can occur. Photons with energy lower than the band gap can not be absorbed, so the material is transparent to these low energy photons.

Energy in excess of the band gap, delivered by the photon to the electron, results in excitation of the electron to a higher energy state in the conduction band and/or a lower energy state of the hole in the valence band. The difference between the photon energy and the material band gap dissipates via interactions with phonons and is converted into heat. It is for this reason that the correct choice of semiconductor material, and corresponding band gap, is crucial. If the band gap is too large, a large portion of the solar spectrum will not be absorbed. If it is too small, the device will absorb more photons but a larger portion of the absorbed energy will be lost to heat. William Shockley and

Hans Queisser calculated the ideal band gap for a single junction PV device to be 1.1 eV,[8] which is one of the reasons that silicon has so extensively been exploited as PV material. For this band gap, the transmittance and dissipative energy losses limit the theoretical achievable efficiency to 30%, the so called Shockley-Queisser limit.

Once excited, the electron-hole pair may be separated either by charge carrier drift, driven by an externally applied voltage, or by random diffusion towards the active area of the p-n junction where the pair is separated by the internal field of the depletion region. Charge is collected at the electrodes at the edge of the device and the energy conversion from light to electrical current is complete.

2.2 Concepts of organic solar cells

Organic semiconductor materials consist of polymers possessing alternating single and double bonds in the carbon backbone. For these materials, the ability to transport charge does not arise from the presence of a valence and conduction band as it does in inorganic semiconductors. Rather, it is possible due to the sp^2 -hybridization in the carbon chain of the polymer. The electron of the P_z -orbital of each sp^2 -hybridized carbon atom will form a so called π -bond with the electrons in the P_z -orbital of the neighboring sp^2 -hybridized carbon atom. This results in a linear chain of sp^2 -hybridized carbon atoms which possess overlapping π -orbitals through which it is possible for electrons to move. The filled π -band is called the Highest Occupied Molecular Orbital (HOMO) while the empty π^* -band is called the Lowest Unoccupied Molecular Orbital (LUMO). In a PV-cell the HOMO of organic materials is analogous to the valence band of inorganic semiconductors and the LUMO is analogous to the conduction band. The difference between the HOMO and LUMO is the band gap of the organic material.

Although charge is able to move through the organic material via the π -orbitals, it is a relatively slow process. Charge mobility for organic semiconductors is typically several orders of magnitude lower than that of inorganic semiconductors with values in the order of 10^{-3} - 10^{-6} $\text{cm}^2 \text{V}^{-1}\text{s}^{-1}$ for amorphous organic films, compared to 6-11 $\text{cm}^2 \text{V}^{-1}\text{s}^{-1}$ for crystallized silicon.[9, 10] Charge mobility plays a significant role in the efficiency of PV devices and part of the challenge in the OPV field lies in overcoming the lack of mobility in organic materials by smart device design. Fortunately, organic materials generally have high absorption coefficients, in the order of 10^5cm^{-1} , [11] giving high absorption even for thicknesses <100 nm, which partly compensates for the low charge mobility as charge does not need to travel very far through the thin film. It also reduces the amount of material needed for the device, which is beneficial when considering production costs.

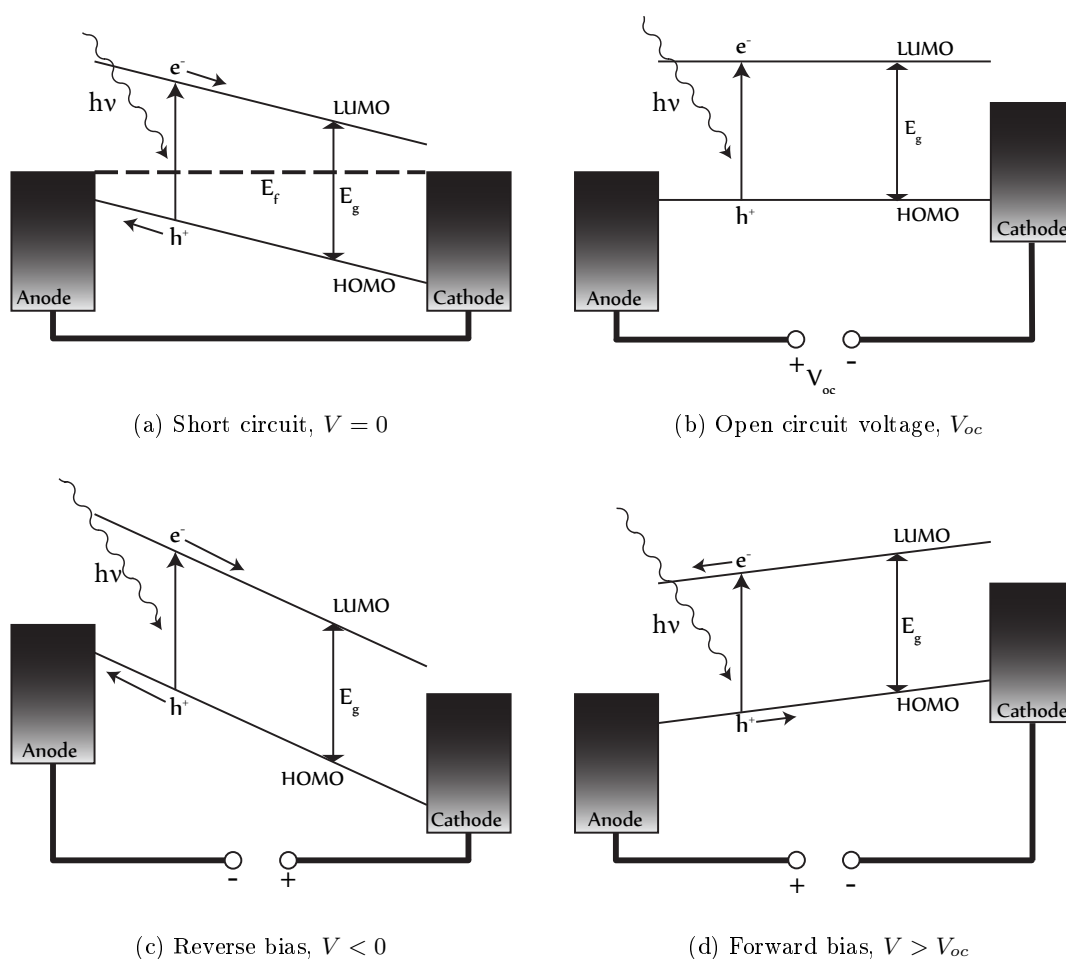


Figure 2.2: Metal-insulator-metal (MIM) picture of organic diode device under diverse bias conditions.

Another crucial difference with respect to crystalline inorganic semiconductors is the fact that light absorbed by organic materials does not result in free charge carriers, but in a tightly bound electron-hole pair called an exciton. This occurs because the dielectric constant of organic materials is relatively low, so that the electric Coulomb force extends over a greater volume than it does in inorganic materials. Another reason is that the non-covalent electron interactions between organic molecules are relatively weak compared to those in covalently bonded inorganic semiconductors such as silicon, causing the electron's wave function to be spatially restricted and allowing it to be localized in the potential well of the corresponding hole and vice versa.[12] The exciton must be dissociated into free charge carriers before extraction can take place. Dissociation mechanisms will be discussed in Sections 2.4 and 2.5. The behavior of organic solar cells under various biasing conditions can be explained using the metal-insulator-metal

model schematically depicted in Figure 2.2. In Figure 2.2a, the short circuit condition is shown. This is the situation where the applied voltage is zero and the current through the device is zero in the dark. If illuminated however, separated charges may drift due to the voltage caused by the difference in work functions of the metal electrode. Holes in the HOMO will drift along the energy band to the electrode with the higher work function, the anode, while electrons in the LUMO will drift to the low work function electrode, the cathode. In Figure 2.2b the situation for open circuit voltage is shown. In this case, the applied voltage exactly cancels out the electric field caused by the difference in work functions of the metal electrodes. Because of this, the energy bands remain flat and the current through the device is zero. The device yields power in the region where the applied voltage is in between short circuit voltage and the open circuit voltage, $0 < V < V_{oc}$. In Figure 2.2c we see the reverse bias situation where only a very small current can flow in the dark but any free charge excited under illumination will be carried to its respective electrode due to the strong field present. The device then effectively functions as a photodetector. Finally, in Figure 2.2d we see the case of a forward bias larger than the V_{oc} . Now, a current flows even in the dark, as the electrodes inject charge carriers into the device. If these charge carriers are allowed to recombine under emission of light, the device then functions as a light emitting diode (LED).

2.3 Device parameter characterization

The ability of a photovoltaic device to convert incident photon energy into electrical energy is characterized by measuring its electrical current output as a function of the externally applied voltage, i.e. its I-V curve. However, the current output of a PV device depends greatly on the active area of the device and it is often more useful to consider the area-normalized current density curve, or the J-V curve. A typical J-V curve is shown in Figure 2.3 This curve can be generated both in the dark and under illumination. In dark conditions, solar cells ideally function as a diode and the current is given by the ideal Shockley diode equation:

$$J = J_0 \left[\exp \frac{qV}{nkT} - 1 \right] \quad (2.1)$$

where J_0 is the saturation current density, n is an ideality factor and k is the Boltzmann constant. The curve shows negligible current in reverse bias and exponentially increasing current under forward bias conditions. Under illumination an additional photocurrent J_{PH} contribution is added and the equation is modified to

$$J = J_0 \left[\exp \frac{qV}{nkT} - 1 \right] - J_{PH} \quad (2.2)$$

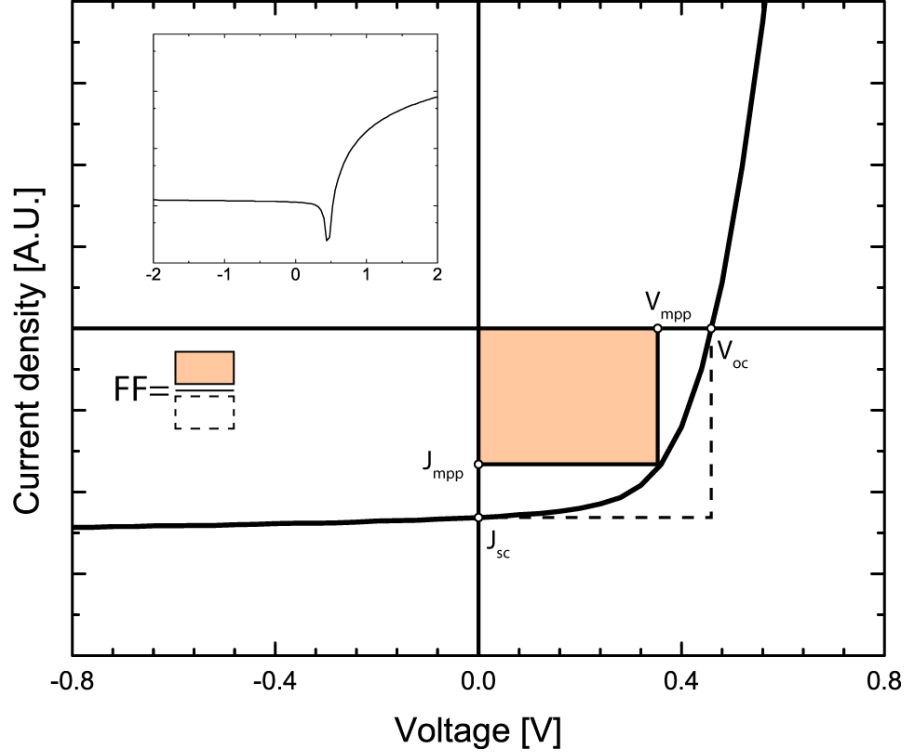


Figure 2.3: A typical J-V Curve. The inset is the same curve on a logarithmic vertical scale.

thus the entire curve shifts downwards. Power can be extracted from the device where the curve is in the fourth quadrant. At negative voltages the J-V curve generally saturates to a maximum current, where the maximum amount of charge carriers are extracted. The maximum electrical power, called the maximum power point P_{mpp} , lies in the fourth quadrant between zero volts (short circuit condition) and the open circuit voltage (V_{oc}). The V_{oc} is the maximum voltage that can be generated by the device and is found where the curve intersects the horizontal axis. From Equation 2.2 we find the V_{oc} to be

$$V_{oc} = \frac{nkT}{q} \ln \left(\frac{J_{PH}}{J_0} + 1 \right) \approx \frac{nkT}{q} \ln \left(\frac{J_{PH}}{J_0} \right) \quad (2.3)$$

The V_{oc} is closely related to the energy diagram of the device. The maximum theoretical V_{oc} is determined by the offset between the quasi-Fermi levels of the positive and negative charge carriers (i.e. the Fermi levels of the charge carriers when their respective populations are displaced from equilibrium). In practice the V_{oc} is also affected by morphological features, non-ideal contacts, and trap states formed at interfaces. [11, 13] Furthermore, it has been found that the V_{oc} is largely independent of the work function of the electrode, and is therefore solely dependent on the energetic and morphologic structure of the active layer.[14]

Another significant point on the J-V curve is the short circuit current density (J_{sc}). This parameter is found at the intersection of the curve and the vertical axis and rep-

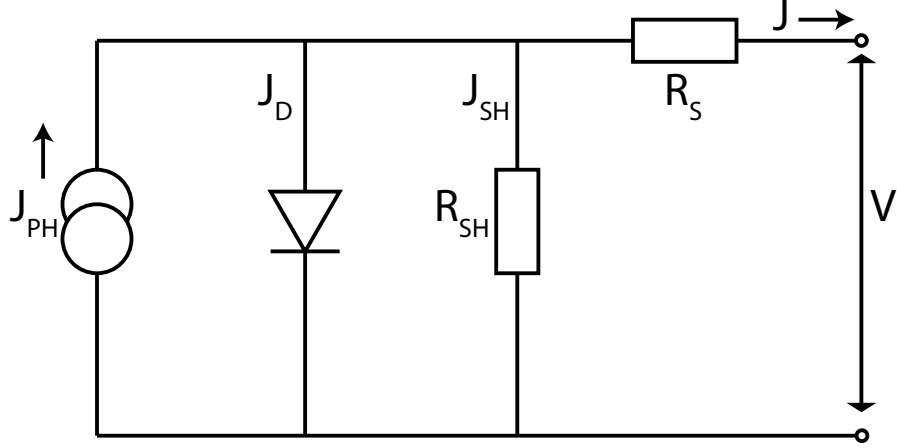


Figure 2.4: Equivalent circuit diagram

represents the maximum photocurrent the device can generate. The short circuit current depends on the density of photons incident on the solar cell, the total absorbance of the device, the overlap of the absorption with the solar spectrum, and the amount of charge carriers lost to recombination before extraction. J_{sc} represents the number of extractable photogenerated carriers, and under monochromatic conditions it can be used to calculate the external quantum efficiency (EQE). EQE is the ratio of the number of incident photons to the number of charge carriers extracted, and is also known as the incident-photon to electron conversion efficiency (IPCE):

$$IPCE(\lambda) = \frac{hc}{q\lambda} S(\lambda) \quad (2.4)$$

where $S(\lambda)$ is the spectral responsivity, i.e. the ratio of the extracted current density to the incident power density at wavelength λ .

Finally, the J-V curve gives us the fill factor FF , which is defined as the ratio of P_{mpp} and the product of J_{sc} and V_{oc} :

$$FF = \frac{J_{mpp} \cdot V_{mpp}}{V_{oc} \cdot J_{sc}}. \quad (2.5)$$

The fill factor is a measure of the quality of the voltage-current characteristics. Ideally, a solar cell would generate the short circuit current for all voltages up to V_{oc} , which would correspond to $FF = 1$. In practice, losses due to recombination account for a decrease in the fill factor. The current voltage properties of a photovoltaic device can be modeled using its equivalent circuit diagram, featuring a current source in parallel with diode. For all practical (non-ideal) devices a series resistance and a shunt resistance need to be added, see Figure 2.4. With these factors the J-V equation then becomes

$$J = J_0 \left[\exp \frac{q(V + JR_s)}{nkt} - 1 \right] - J_{PH} - \frac{V + JR_s}{R_{sh}} \quad (2.6)$$

where R_s and R_{sh} are the series and shunt resistance respectively. The series resistance takes into account the nonzero resistance encountered during bulk-transport, interface-transport and charge transfer to the electrodes, while the shunt resistance accounts for current leaks due to recombination. Therefore to obtain a high fill factor, one must strive for a very low series resistance in combination with a very high shunt resistance.

The overall efficiency η of a solar cell under solar intensity P_{solar} is given by

$$\eta = \frac{J_{sc} \cdot V_{oc} \cdot FF}{P_{in}} \quad (2.7)$$

Strong interdependencies between the factors in the numerator mean that high efficiency can only be reached by joint optimization of J_{sc} , V_{oc} , and FF .

2.4 Schottky junction devices

Excitons form an important intermediate step in the energy conversion process. They are bound by the electrostatic Coulomb force between the negatively charged electron and positively charged hole. This force needs to be overcome for the exciton to be dissociated into free charge carriers. Exciton dissociation can take place if an electric field is present strong enough to overcome the binding energy of the exciton, typically 0.2-1 eV in organic materials.[15] In a single material device this can occur by field-assisted charge separation at a Schottky barrier, see Figure 2.5. A Schottky barrier forms when a semiconductor

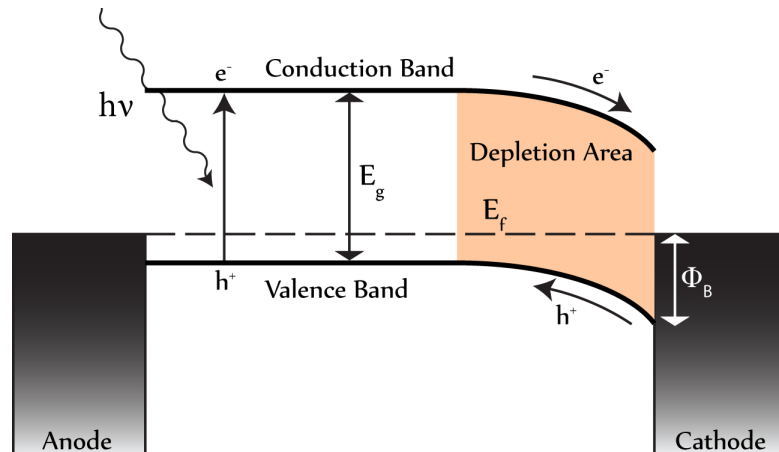


Figure 2.5: Band energy diagram of a p-type Schottky device

and metal with different work functions are brought into ohmic contact with each other. If the circuit is closed (for example by an external wire) electrons will flow from high work function material to the low one until the Fermi levels are aligned. This causes a depletion region to be formed and results in a built in potential on the semiconductor side of the metal-semiconductor interface. This potential may be strong enough to overcome the exciton binding energy and facilitate dissociation to occur. Devices which rely on this

principle are frequently called Schottky-junction devices and are not limited to organic devices, but also feature prominently in colloidal quantum dot (CQD) based devices, such as the lead-salt nanocrystals which are investigated in this research.

Schottky devices have the advantage of straightforward device fabrication, but there are several factors which limit the device efficiency:[16]

- Schottky-junction devices are exciton diffusion limited. Light intensity decreases as it travels through the active layer of the device, in accordance with Beer-Lamberts law. As a consequence, most excitons are formed near the transparent ITO electrode and must travel through the active layer to the electron-collecting Schottky contact where the band bending is greatest and dissociation is most likely to occur. Due to the long travel distance these carriers are vulnerable to recombination.
- For an ideal Schottky junction, the height of the energy barrier Φ_B at the metal-semiconductor interface (Figure 2.5) is limited to $\sim 0.67E_g$.[16] In practice however, Schottky devices suffer from Fermi-level pinning due to defect states at the interface leading to a decrease in V_{oc} .
- The barrier to hole-injection at the electron collecting contact is not very large, allowing back-recombination to occur which limits shunt resistance and causes a drop in fill factor.

The most successful active layers in Schottky devices have been fabricated by depositing p-type NCs in a layer-by-layer fashion, either by dipcoating or spin coating.[17–19] Indium tin oxide (ITO) has become widely used in optoelectronic devices due to its combination of excellent conductivity and high optical transparency, and is used throughout this study as the hole-collecting electrode of our devices.

2.5 Hybrid solar cell devices

As mentioned in Section 2.2, one of the challenges that needs to be overcome in organic photovoltaic cells is achieving efficient exciton dissociation. In this section we will discuss the dissociation mechanism by means of a donor-acceptor heterojunction. Specifically, using inorganic PbS NCs as donor and an organic semiconductor material as acceptor. PV devices which employ both inorganic and organic semiconductors are often referred to as ‘hybrid’ solar cells. There are two hybrid structures we will discuss in turn, bilayers and bulk-heterojunctions.

2.5.1 Bilayer heterojunction solar cells

In Section 2.2 we discussed the mechanism of exciton dissociation at a Schottky barrier. For single material OPV devices this process is the most prominent means of exciton dissociation. Often however, the built in fields created by Schottky barriers are often not strong enough for efficient dissociation to take place. For this reason, devices with more than one active material are interesting, as the interface between the two materials forms a site where exciton dissociation can take place. The simplest of these structures is the bilayer. A bilayer device employs a single heterojunction between a planar donor and acceptor layer, which are sandwiched between two electrodes (Figure 2.6a). If the two semiconducting materials, one with a high electron affinity (the acceptor) and a one with a low electron affinity (the donor) are brought in contact with each other, they may form a so called type-II heterojunction, in which the LUMO (in the case of organic materials) of the acceptor is lower than that of the donor and the HOMO of the acceptor is lower than that of the donor, Figure 2.6b. Unlike the classical p-n junction, which requires doped semiconductors with free charge carriers to form the depletion region which generates an electric field, exciton dissociation at a bilayer-heterojunction takes place due to the differences in the ionization potential and electron affinity of the adjacent materials. If an acceptor material is near, an electron in the LUMO of the donor may be transferred to the LUMO of the acceptor, provided that the electron affinity A_A of the acceptor is great enough to satisfy: $A_A > I_{D^*} - U_C$, where I_{D^*} is the ionization potential and U_C is the effective Coulomb interaction between the charge carriers.[20] For efficient charge carrier transfer to the electrodes, the anode should match the HOMO of the donor and the cathode should match the LUMO of the acceptor.

The fabrication of bilayers is relatively straightforward and can be achieved by sequentially spin coating layers of semiconductor material, provided the first layer is not soluble in the solvent of the second.

A major advantage of bilayer devices with respect to single layer devices lies in the fact that after dissociation and during subsequent transport to the contacts, the charge carriers are effectively separated from each other. The electron travels through the mostly hole-free acceptor material and the hole travels through the electron-free donor, greatly reducing the probability of recombination events, which is then dominated by trap densities. Because of this, high fill factors can be expected in bilayer devices. A disadvantage is that, much like Schottky-junction devices, bilayer structures are still exciton diffusion limited. Excitons formed by photon absorption must travel to the heterojunction interface by random diffusion. Because the diffusion length of most organic materials is below 20 nm, only excitons formed within this distance of such an interface contribute to the photocurrent.[7] Excitons formed outside this region will recombine and

the excitation energy will be lost. To prevent this, it is desirable to have a heterojunction interface within the exciton diffusion length at every point in the active layer. This can be achieved in a bulk-heterojunction, which will be discussed in the next section.

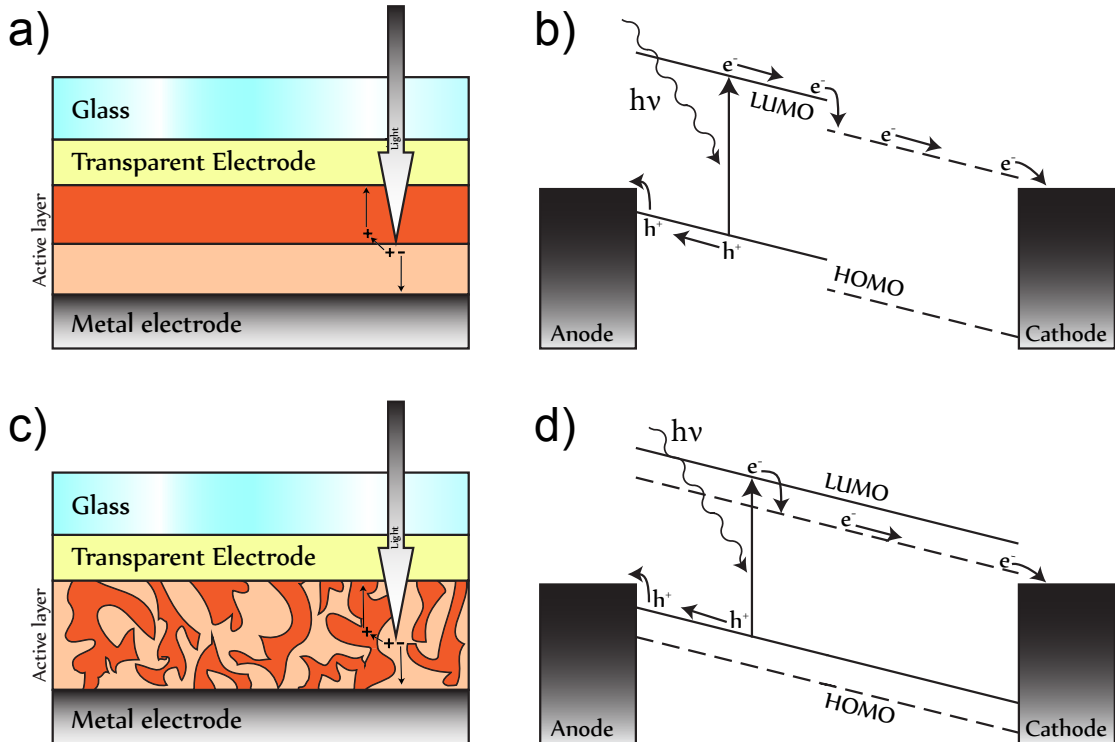


Figure 2.6: (a) Bilayer device structure. (b) Bilayer energy bands under short circuit conditions. (c) Bulk-heterojunction device structure. (d) Bulk-heterojunction energy bands under short circuit conditions.

2.5.2 Bulk-heterojunction solar cells

The term bulk-heterojunction implies that these device structures aim to have a type-II heterojunction interface throughout the bulk of the active layer, so that all excitons formed by photon absorption lie within the exciton diffusion length of a dissociation facilitating interface. Unlike bilayer devices, where donor and acceptor materials are fully in contact with their corresponding electrodes, bulk-heterojunction devices require percolated pathways along which charge carriers can be transported to the contacts. The greatest challenge of bulk-heterojunction devices is therefore controlling the nanoscale morphology in such a way that a bicontinuous and interpenetrating network of donor-acceptor phases is formed. Nevertheless, bulk-heterojunction structures are considered the ideal system for thin film photovoltaic applications. The interpenetrating network of two components leads to an extremely large interfacial area together with an efficient, homogeneous charge generation throughout the device. Bulk-heterojunction devices may be fabricated by spin coating a blend of donor-acceptor materials, although the measure

in which percolation pathways are formed depends strongly on the miscibility of the donor and acceptor materials, the spin coating recipe and other process steps such as annealing. If achieved however, energy loss due to recombination will greatly be reduced. Practically all excitons can be dissociated and, once separated, charge carriers are transported within their respective phases and do not encounter carriers of the opposite charge with which they can recombine. One may therefore expect a high photocurrent as well as fill factor.

2.6 Nanocrystals as PV material

In this section we will discuss the characteristics of inorganic semiconductor nanocrystals, specifically chalcogenide lead sulfide nanocrystals, as these were used in all device structures presented in this study. NCs are crystal materials consisting of a few hundred to a few thousand atoms aggregated in a cubic NaCl crystal structure.[21] In recent times, they have attracted a lot of interest in the field of optoelectronics due to their unique optical and electronic properties resulting from their size. Typical NC dimensions range from 1-10nm, in between that of discrete molecules and microorganisms, see Figure 1.1. This places them in a very interesting size-regime where the electronic properties of

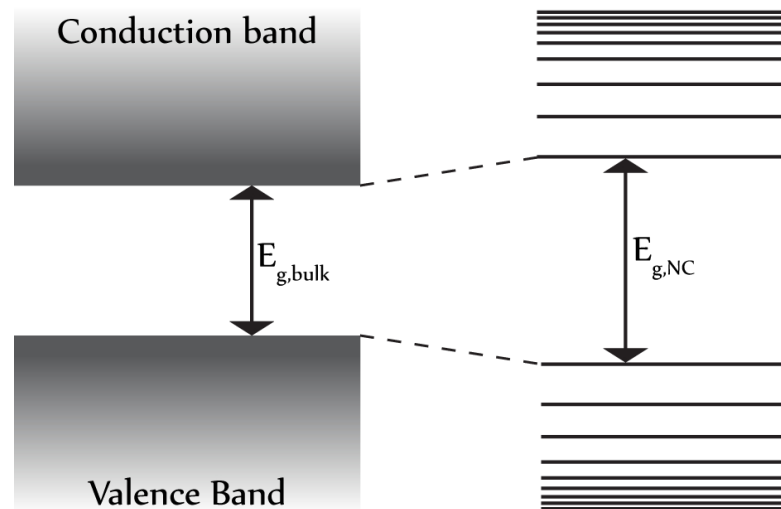


Figure 2.7: Schematic energy band diagram for bulk (left) and quantum dot (right), figure is not to scale.

the NCs lie somewhere between that of a bulk semiconductor and individual molecules. In bulk semiconductors, the conduction electrons are free to move around and have a continuous energy spectrum. If one decreases the size of the semiconductor to such an extent that the electron is confined in all three dimensions, a so called quantum dot, the continuous spectrum will become discrete and the band gap will increase (Figure 2.7). This quantum confinement effect occurs when the semiconductor is of comparable size or smaller than the Bohr radius of an electron-hole pair. For PbS, the Bohr exciton

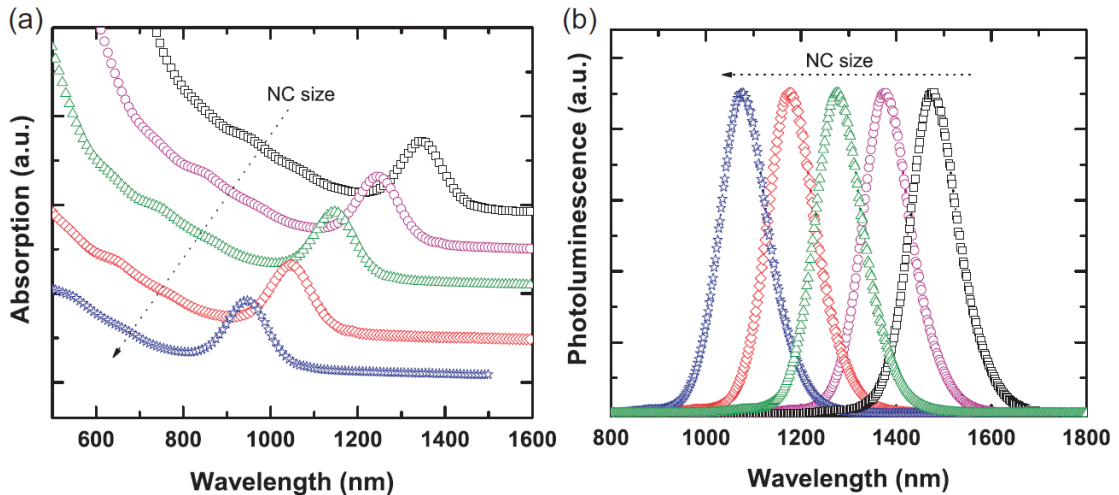


Figure 2.8: Absorption and photoluminescence spectra of PbS NCs with sizes ranging from ~ 3.8 to ~ 5.0 nm. [24]

radius is ~ 20 nm and the NCs investigated in this research are between 3-5 nm in diameter, which places them in the extreme quantum confinement regime.[21, 22] To illustrate this, the band gap of bulk PbS is 0.41 eV whereas the band gaps of the NCs used in this study is 1.1-1.3 eV, thus the band gap energy in our PbS based devices is dominated by quantum confinement.[22, 23] The size dependence of the quantum confinement effect is one of the greatest advantages of NCs in photovoltaic devices because it leads to an enhancement of the absorption, allowing thinner films, and it allows the energy band gap to be tuned by varying the diameter of the NCs. This allows optimization of the band gap for both single-junction and multi-junction device architectures. It also opens the window to achieve photoexcitation in parts of the solar spectrum that were previously unharvestable, especially at longer wavelengths in the infrared region, as demonstrated in Figure 2.8. These optical properties are nicely complemented by beneficial electronic properties. The large exciton Bohr radius in PbS, in combination with small effective masses of charge carriers ($\sim 0.09m_e$) promotes charge delocalization in NC films, resulting in an increased charge carrier mobility compared to bulk materials of the same type.[21]

Nanocrystals properties are not only determined by size and material type, but in large part also by their surface chemistry. To stabilize the crystal structure and prevent oxidation, PbS NCs are capped with oleic acid ligands during fabrication. These ligands have many beneficial aspects, such as preventing aggregation, reducing reactivity in ambient conditions and facilitating solubility in organic solvents. However, they have the disadvantage of being long, insulating molecules which adversely affect electric properties by forming barriers to charge transport between NCs. For efficient charge transport, the ligands must therefore be replaced by shorter molecules such as the bilinging 1,4-

benzenedithiol (BDT), seen in Figure 3.2, by exposing the nanocrystal film to the bilinker after deposition. BDT has two adjacent sulfur groups on either side of the benzene ring which form strong bonds with the PbS NCs, replacing the existing ligands and crosslinking neighboring nanocrystals. In doing so, the insulating molecules are removed and the inter-NC distance is decreased, see Section 4.4, which leads to much improved charge transport characteristics.[25]

It has been reported that the width of the depletion region in PbS Schottky devices lies between 150-200 nm, so we assume all our PbS-only devices are fully depleted.[22, 26] This is important because charge carriers generated in the depletion region are collected with much higher efficiency than those generated in the quasi-neutral region, as there very little chance of them recombining with mobile charge carriers of the opposite type. It also implies that there is a built in electric field throughout the bulk of the layer which can facilitate exciton dissociation and drive charge carrier drift.

All in all, PbS NCs offer a beneficial combination of optical and electrical properties, as well as a high degree of adaptivity, making them an extremely interesting candidate for second generation solar cell applications.

Methods

In this chapter the methods and details of our experiments will be discussed. First, a description of all the materials used in the fabrication of our devices will be given. After that, the fabrication process itself will be discussed. Finally, we will give a description of the experimental setups used to measure and characterize our samples.

3.1 Materials

The devices investigated in this study are all thin film CQD-based solar cells, in which an active layer is sandwiched between two electrodes in a planar fashion. The active layer itself consists of one or more layers of photoactive materials, forming either a single-layer, bilayer, bulk heterojunction, or a combination thereof. In all cases the active layer is deposited on the substrate by consecutively spin coating one or more layers of active material from the bottom up. We will briefly discuss the properties and function of the relevant materials in this section.

3.1.1 Glass and ITO

All the devices considered in this study were fabricated on glass substrates onto which areas of Indium Tin Oxide (ITO) have been deposited, see Figure 3.3. These substrates are ready made by Philips Research Laboratory and need only minimal preparation before use. Glass is an ideal substrate for our purposes because of its flatness, rigidity and of course its transparency in the spectral range of interest, i.e. visible and infrared.

The use of ITO has become widespread in optoelectronic devices because of its relatively high work function of ~ 4.8 eV, which makes it very suitable as a hole-extracting electrode.[27] Furthermore, ITO is highly transparent, which allows it to be used on the side of the device on which the light is incident, without shadow effects limiting device efficiency. Its high conductivity allows charge to be carried away efficiently and the high

atmospheric stability and insolubility of the ITO surface allows it to be used in ‘wet’ processing conditions during cleaning and spin coating and even allows the substrate to be cleaned and reused, provided the active layer is soluble and can be completely removed.

3.1.2 PbS nanocrystals

Chalcogenide lead-sulfide nanocrystals are the focus of this study and form a component in all the investigated devices. As mentioned in the previous chapter, PbS is a promising material for PV devices due to its high absorption coefficient, good conductivity and tunability of the band gap. PbS NCs exhibit good solubility in most non-polar solvents such as toluene, chlorobenzene and chloroform. The NCs used in this study were synthesized by hot injection method and were capped by oleic acid ligands to improve stability and prevent aggregation.[28] During the synthesis of the NCs one or more washing steps were performed to get rid of surfactants and excess ligands. However, it is possible that some surfactants and ligands still remain in the solvent, which may affect device performance. In this study NCs were used featuring sizes ranging from ~ 3.8 nm to ~ 4.3 nm in diameter, resulting in NCs with first excitonic peaks of 980 nm to 1110 nm respectively.

3.1.3 1,4-Benzenedithiol

As a bilinker molecule 1,4-benzenedithiol (BDT) was used. This aromatic molecule consists of a benzene ring with two adjacent sulfur groups on either side. BDT possesses a higher affinity to the NC surface than the carboxyl group of oleic acid and can therefore displace these molecules. In doing so, the sulfur groups of BDT bond with the surface of the PbS crystals, crosslinking neighboring particles, see Figure 3.1. During the layer-by-layer deposition of PbS, ligand exchange was achieved by soaking the active layer with a solution of BDT for a fixed time period in between each deposition. At room temperature, BDT is a solid and is readily soluble in acetonitrile.

3.1.4 [6,6]-phenyl-C61-butyric acid methyl ester

Often referred to as PCBM, [6,6]-phenyl-C61-butyric acid methyl ester is a fullerene derivative of the Buckminsterfullerene (C60) molecule, see Figure 3.2. Due to its high electron affinity and relatively good conductivity this molecule has attracted much interest in the OPV field as an electron acceptor in bilayer or bulk-heterojunction devices. PCBM has energy levels of 6.1 eV and 3.8 eV for the HOMO and LUMO respectively, thus exhibiting a band gap of 2.3 eV.[29] High electron affinity and conductivity notwithstanding, the large bandgap of PCBM results in a very low absorption coefficient. Com-

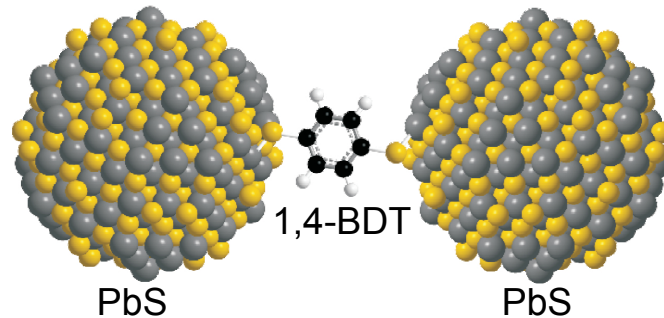


Figure 3.1: Schematic depiction of two NCs crosslinked by 1,4-BDT. The two sulfur groups on either side of the BDT molecule attach to the Pb atoms on the surface of neighboring particles. This figure is not to scale.

binning this material with PbS nanocrystals solves this problem, as the NCs particularly high absorption coefficient provides sufficient light absorption. PCBM is preferred over the plain C60 molecule because its solubility in common organic solvents is significantly higher, making it more practical and suitable to solution-based processing methods such as spin coating. More specifically, it is readily soluble in chloroform, which allows it to be mixed with PbS in solution for the production of bulk-heterojunction structures.

3.1.5 Poly(3-hexylthiophene)

This high band gap (1.9 eV) polymer, commonly referred to as P3HT, has been widely researched and used very successfully in combination with other organic materials. In combination with PCBM, efficiencies of almost 5% have been achieved, which is exceptional for organic PV devices.[30] With energy levels at 2.7 eV and 4.8 eV it forms a type-II heterojunction with both PCBM and PbS NCs and the HOMO level is just high enough to achieve hole-injection into the anode (ITO), making it an interesting material to explore.

3.1.6 PCPDTBT

Poly[2,6-(4,4-bis-(2-ethylhexyl)-4H-cyclopenta[2,1-b;3,4-b']dithiophene)-alt-4,7(2,1,3-benzothiadiazole)], also known as PCPDTBT is an interesting polymer to consider in OPV applications. It possesses a band gap of 1.4eV and also forms a type II-heterojunction with PbS,[31] although in this case PbS is now the electron acceptor, and it is interesting to study how well it performs in such a role. Devices employing a bulk-heterojunction of PCPDTBT in combination with PCBM have found to yield efficiencies of 3.2%.[32, 33] Potentially, sensitizing such a device with PbS nanocrystals could improve this performance.

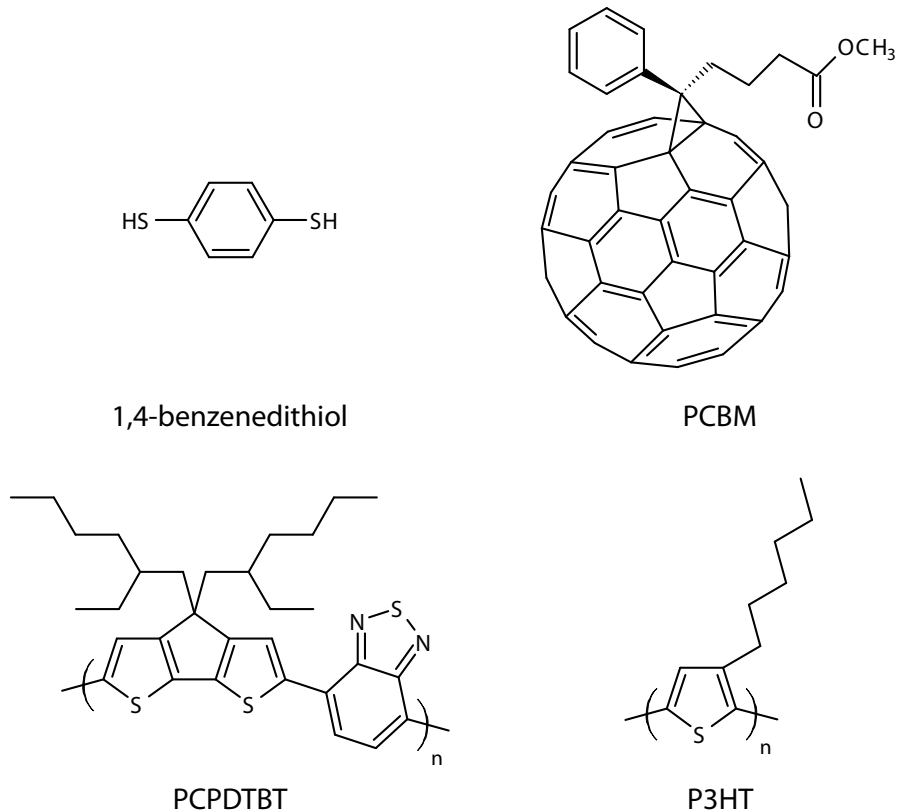


Figure 3.2: Molecular structure of organic materials used in device fabrication.

3.1.7 Aluminium and lithium fluoride

Throughout this study aluminium is used as the cathode due to its work function of 4.3 eV, which is lower than the LUMOs of all the materials mentioned above, making it a suitable electron extracting material.

In studies such as Tang et al. it was found to be beneficial to add a thin ($\sim 1\text{nm}$) layer of LiF in between the active layer and the aluminium electrode.[34, 35] This interstitial layer has been reported to improve device performance, reducing series resistance at the PbS-Al interface and increasing overall shunt resistance by delaying the diffusion of oxygen at the NC-metal junction. This prevents the formation of trap states due to oxidation of the Al interface and increases device lifetime.

3.1.8 Solvents

The samples researched in this study were fabricated using solution based methods such as spin coating and dropcasting. Prior to the deposition of the active layer, the photoactive materials must therefore be dissolved. For this purpose, several organic solvents were used, which will be discussed in this section.

Toluene

Toluene is a common, colorless, non-polar solvent. The PbS nanocrystals used in this study were delivered in highly concentrated solutions of toluene as the NCs were found to be the most stable and possess the highest longevity in this solvent. Toluene has a high boiling point (110.6°C), which is good in terms of stability, but due to its relatively low vapor pressure it was not ideally suited to our layer-by-layer deposition method. Therefore, prior to device fabrication, the NC solvent was changed to Chloroform.

Chloroform

Chloroform is a volatile, colorless solvent that provides good solubility for a wide range of organic materials, including PCBM, P3HT, PCPDTBT, and NCs capped with oleic acid ligands. It is largely unreactive and due to its low boiling point (61.2°C) it possesses a uniquely high vapor pressure among organic solvents. Because of its volatility, it has become widely used in wet processing methods as it dries quickly, conveniently shortening processing times. At the same time however, it increases the difficulty of obtaining a uniform coverage of the substrate.

Acetonitrile

Also a colorless organic solvent, acetonitrile was used to dissolve the bilinker BDT, prior to device fabrication. With a boiling point of 82°C, it is sufficiently nonvolatile to be used in a soaking step for ligand exchange.

3.2 Device fabrication

During device fabrication it is imperative that contamination of dust particles is kept to a minimum. Dust particles sizes are typically in the order of $\sim 1 \mu\text{m}$ and are thus several factors larger than our total device thickness. Therefore, a dust particle on the substrate may be significantly detrimental to device performance, and may even cause the device to short circuit. To avoid this, all procedures relating to device fabrication took place in a cleanroom of class 10,000 (US FED 209E standard), meaning that there is a maximum of 10,000 particles of size $\geq 0.5 \mu\text{m}$ per cubic foot. This is equivalent to a grade 6 in the ISO 14644-1 cleanroom standards. In this section we will present the details of each processing step in the order they take place during fabrication.

3.2.1 Fabrication steps

Substrate preparation

Prior to device fabrication, two preparatory steps need to be taken, the first is substrate

preparation. The substrate consists of a piece of glass of dimensions 3×3 cm with pre-deposited ITO contacts. This substrate is cleaned according to a well-tested procedure in which each sample is first scrubbed manually with a warm ($\sim 50^{\circ}\text{C}$) solution of soap and deionized water (DI water) for about 5 minutes using plastic scrubbing gloves. This step is instrumental in achieving a smooth surface, removing spikes in the ITO layer which may cause the device to short circuit. The substrate is then rinsed in a flow bath of DI water for 7 minutes, then cleaned with acetone in an ultrasonic bath for 5 minutes to remove any organic materials, rinsed again for 7 minutes in the flow bath and then rinsed of any remaining acetone in 2-isopropanol for an additional 5 minutes under sonic vibration. A 10 minute drying step takes place after this in an oven at 140°C in ambient conditions, followed by a UV-ozone treatment for 20 minutes. During this cleaning procedure, the substrate is constantly kept in a class 1,000 air flow (ISO 7).

Solution preparation

The other necessary step prior to device fabrication is the preparation of the solutions. In general, this is done by weighing out the material, and subsequently adding an appropriate amount of solvent to achieve the desired concentration. The material is weighed on a scale sensitive to 10^{-4} g and solvent is added by pipet. This is followed by prolonged stirring using magnetic stir-bars on a magnetic plate for a period ranging from 30 minutes to several hours, depending on the solvent and material. If necessary, the magnetic stir plate is heated (not higher than 50°C) to accelerate the dissolving rate. For practical reasons, solutions were often prepared the previous day and left to stir overnight. This was particularly necessary for the solution of BDT in acetonitrile, as it took several hours to dissolve satisfactorily.

Due to the high volatility of chloroform, solutions based on this solvent are always prepared the same day as device fabrication to maintain a well-defined concentration. Solutions are then filtered to extract any aggregates or impurities that may still be in solution.

Solvent exchange

The PbS NCs are delivered in a highly concentrated solution of toluene, and it is first necessary to change solvents. This is accomplished by extraction of the toluene by rotary evaporation, after which the NCs were re-dissolved in chloroform to make a highly concentrated stock solution from which lower concentration solutions were prepared.

Deposition of the active layer

With a clean substrate and prepared solutions, the actual processing steps can take place.

The active layer of the solar cell is deposited by spin coating. Spin coating is a commonly used processing method used to produce uniformly thin films on flat substrates. In this process, an excess amount of solution is first deposited on the substrate, which is placed in a holder. The substrate is then subjected to high speed rotation and the fluid is spread across the substrate by the centrifugal force. This process can be divided into several stages that determine the final film characteristics. Directly after deposition but before rotation, the spreading of the solution over the substrate is dominated by the wetting properties of the liquid on the substrate surface, and by subsequent evaporation of the solvent. The latter is of particular importance for solvents with a high vapor pressure, such as chloroform. As the solvent evaporates, the pool of solution on the substrate shrinks, leaving behind undesirable residual rings of photoactive material. To ensure uniformity of the active layer it is therefore essential to keep this stage as short as possible, and to initiate rotation directly after deposition. In doing so, we assume that this stage does not affect our layer quality. The next stage is a period of acceleration until the final speed is reached. Usually this stage is kept short, lasting only a couple of seconds. During the first part of the next stage, the stage of constant spinning speed, the fluid thinning behavior is dominated by fluid viscous forces. Final thickness is for the most part determined during this period and is greatly dependent on the speed of rotation, as well as the initial concentration of the solution. As the fluid is spread out over the substrate and the layer becomes thinner, the influence of viscous forces decreases and the effect of solvent evaporation starts to dominate the film thinning behavior. The spin coater is equipped with a lid that can be left open or closed during operation. Closing the lid induces a vapor rich environment which leads to a slower evaporation rate and in general leads to smoother, more uniform layers. Rotation is maintained until it is certain that all the solvent has been evaporated. This is especially important in a layer-by-layer method, as the deposition of material on top of a layer containing residual solvent may trap the solvent in the active layer and affect device performance. To summarize, the thickness and quality of the active layer are predominantly determined by the combination of four factors: type of solvent, solution concentration, spin duration and acceleration speed. All spin coating steps were performed in a nitrogen-filled glove-box, constantly filtering out oxygen and water to strictly maintain levels of <0.1 ppm O_2 and H_2O . For the layers containing PbS, spin coating was followed by an annealing step, which is believed to facilitate phase segregation in bulk-heterojunction devices and has been found to be beneficial to the performance of PbS layers as well. [35, 36]

Layers of PbS NCs are deposited using a layer-by-layer method in which a film of PbS is deposited onto the substrate by spin coating at 4000 rpm for 60 seconds, from a 5 mg/ml chloroform solution. This is followed by a ligand exchange step in which the PbS

film is soaked in a 0.02 M solution (2.8 mg/ml) of 1,4-BDT in acetonitrile for 30 seconds and subsequently spun once more at 4000 rpm for 60 seconds to remove the solution from the surface. During the soaking step the layer becomes insoluble in chloroform due to the removal of the soluble oleic acid ligands and crosslinking of PbS particles. This allows another layer to be deposited on top and the process to be repeated until the desired thickness is achieved. A single film of PbS deposited in this manner is roughly 6-7 nm thick.

Other layers consisting of organic materials or a mix of organic with PbS NCs are fabricated in a single step spin program, the details of which are given in the following section.

After the active layer has been deposited, a 10 minute annealing step is performed at 140°C.

Thermal evaporation of top contact

Without leaving the nitrogen environment, the samples are transferred from the spin coater to a vacuum chamber (10^{-6} - 10^{-7} mBar). Here the devices are finished by thermal evaporation of the metallic cathode, consisting of a 1 nm layer of LiF followed by 100 nm of aluminium. To accomplish this, the device is suspended above a conductive boat containing small shards of the electrode material. A current is then fed through the boat, heating the electrode material to the point at which it evaporates upwards onto the device surface. A mask with four slots, one for each device area, is used to ensure that the metallic electrodes are deposited perpendicularly to the ITO areas, such that both electrodes can be accessed, see Figure 3.3.

TEM sample preparation

To analyze the effect of ligand exchange on inter NC separation, images of nanocrystal arrays are made using transmission electron microscopy (TEM). To achieve this, we use a carbon grid substrate, consisting of many thin films of carbon, suspended between a metallic grid. A layer of nanocrystals is deposited onto the substrate by drop casting, depositing one or more droplets of solution onto the substrate and letting the solvent evaporate in a fume hood. Images are made both of NCs capped with oleic acid ligands (o-PbS), and NCs soaked in a 0.02 M solution of 1,4-BDT in acetonitrile for 15 seconds (PbS-BDT).

3.2.2 Device recipes

In this section a summary of device fabrication processes will be given. All devices are made using the same glass-ITO substrates, prepared with the same cleaning process

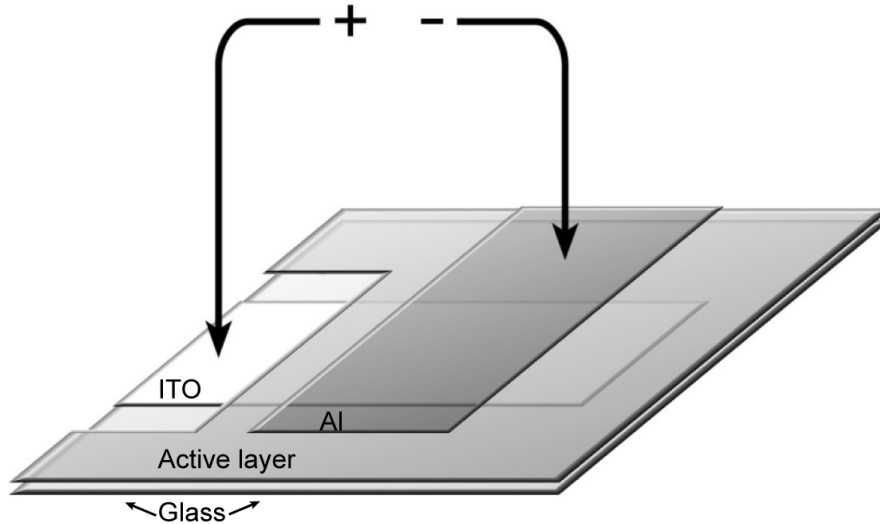


Figure 3.3: Configuration of a PV cell. The active layer is partially removed to clear the transparent ITO anode. A DC-voltage is applied across the anode and the metal cathode. The active area is where the electrodes overlap each other. Each device contains four differently sized active areas.

and finished with the same cathode deposition method, so the devices have a general structure ITO/Active layer/LiF(1nm)/Al(100nm) and differ only in the structure of the active layer. Before deposition, solutions were passed through a size-limiting particle filter to extract any aggregates or impurities from the solution. The filters used in the different solutions are displayed in Table 3.1.

Material	Solvent	Filter
PbS NC	chloroform	5.0 μm
P3HT	chloroform	5.0 μm
PCPDTBT	chloroform	0.45 μm
PCBM	chloroform	0.2 μm
PbS NC + P3HT	chloroform	5.0 μm
PbS NC + PCPDTBT	chloroform	0.45 μm
Pbs NC + PCBM	chloroform	0.2 μm
1,4-BDT	acetonitrile	1 μm

Table 3.1: Filters used prior to active layer deposition

A summary of device recipes used in this study is presented below. Spin programs are characterized by their speed of rotation, acceleration, lid position and duration respectively. Layer structures are presented in order of deposition, i.e. from the bottom up.

PbS Schottky device

Active layer structure: PbS-NC

- – For 80 nm device: spin coat 15 films of BDT treated PbS
- For 150 nm device: spin coat 25 films of BDT treated PbS
- Anneal at 140°C for 10 minutes

PbS-PCBM bilayer device

Active layer structure: PbS-NC(40 nm)/PCBM(40 nm)

- Spin coat 15 films of BDT treated PbS
- Anneal at 140°C for 10 minutes
- Spin coat PCBM(10mg/ml) in chloroform at 1500 rpm, 1000 rpm/s, with lid closed for 60 seconds

PbS-PCBM bulk-heterojunction device

Active layer structure: PbS-NC(40 nm)/PbS:PCBM(40 nm)/PCBM(40 nm)

- Spin coat 8 films of BDT treated PbS
- Spin coat PbS-NC(20mg/ml) : PCBM(0.66mg/ml) blend in chloroform at 2200 rpm, 1000 rpm/s, with lid closed for 60 seconds
- Anneal at 140°C for 10 minutes
- Spin coat PCBM(10mg/ml) in chloroform at 1500 rpm, 1000 rpm/s, with lid closed for 60 seconds

Bi-blend device

Active layer structure: PbS-NC:P3HT(100 nm)/PbS-NC:PCBM blend(40 nm)

- Spin coat 7 films of PbS-NC(10mg/ml):P3HT(1.5mg/ml) blend at 1300 rpm, 1300 rpm/s, with lid closed for 60 seconds, then soak in BDT for 5 minutes
- Spin coat PbS(20mg/ml):PCBM(0.66mg/ml) blend in chloroform at 2200 rpm, 1000 rpm/s, with lid closed for 60 seconds
- Anneal at 140°C for 10 minutes

PbS-PCPDTBT bulk-heterojunction device

Active layer structure: Active layer structure: PbS-NC:PCPDTBT (140 nm)

- Spin coat PbS(20mg/ml):PCPDTBT(0.8mg/ml) blend in chloroform at 4000 rpm, 4000 rpm/s, with lid closed for 60 seconds

3.3 Measurement techniques

3.3.1 J-V characteristics

The J-V characteristics are perhaps the most important aspect of a PV device, as they not only determine the overall efficiency, but from it insights into the inner mechanisms of the solar cell can be deduced as well. After completing the fabrication process, the device samples are transported out of the cleanroom to another nitrogen-filled glovebox. This is done in a sealed steel container, allowing a nitrogen environment to be maintained throughout transportation. In this glovebox the device performance is determined by measuring its current response to an applied DC-voltage, both in the dark and under illumination. The device is placed in a sample holder possessing eight contact points, which match the positions of the cathode and anode for all four device areas. Since the ITO is now covered by the material of the active layer, it must first be uncovered by carefully scratching off the semiconducting material with a small scalpel at the contact points. A mask with slightly smaller apertures than the device area is placed over the sample to eliminate current contribution from regions beyond the anode/cathode overlap and ensure a well-defined device area. As a light source, a Steuernagel SolarConstant 1200 metal halide lamp is used. Using a Si cell with well-known characteristics as a reference, the lamp is calibrated to 1 sun intensity (1000 W/m^2) in accordance with standard testing conditions. However, the spectrum of the lamp differs from the standard Air Mass 1.5 Global (AM1.5G) solar spectrum, which is the solar spectrum of the sun after passing through 1.5 atmospheric thicknesses, and we must make a correction for the spectral mismatch. This mismatch factor is given by

$$M = \frac{\int E_R(\lambda)S_R(\lambda)\delta\lambda}{\int E_S(\lambda)S_R(\lambda)\delta\lambda} \cdot \frac{\int E_S(\lambda)S_T(\lambda)\delta\lambda}{\int E_R(\lambda)S_T(\lambda)\delta\lambda} \quad (3.1)$$

where E_R and E_S are the spectral radiance distributions of the Air Mass 1.5 Global (AM1.5G) reference spectrum and solar simulator respectively, and S_R and S_T are the spectral responsivities of the Si reference cell and test cell respectively. The spectral responsivities are obtained during measurements of the external quantum efficiency, described in the following section. The temperature of the device is kept constant using a manually controlled nitrogen flow which is passed through a bath of liquid nitrogen. All measurements are performed at a temperature of 295°K , which we refer to as room temperature. A variable DC-voltage is applied to each device area in turn. The J-V output is measured by a Keithly 2400 Sourcemeter and the data is recorded by a computer using National Instruments LABVIEW software. The current response is measured by varying the voltage in steps of 0.04 V from 0 V to 2 V, then down to -2 V and back to 0 V, effectively sweeping the range -2 - 2 V twice, once in forward direction and

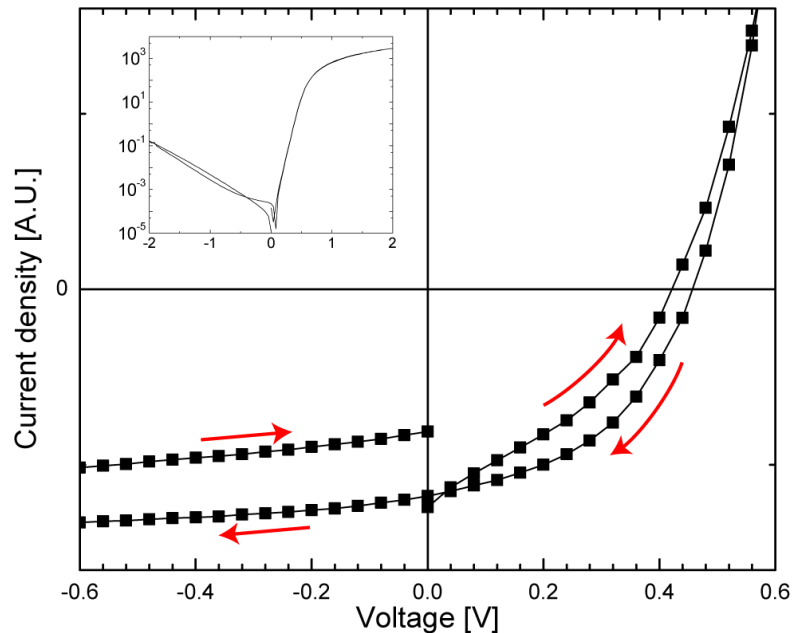


Figure 3.4: Typical J-V curve displaying significant hysteresis.

once backwards. This is done separately for all four device areas, both in the dark and under illumination. A typical J-V curve is given in Figure 3.4. An interesting feature of these curves is the hysteresis. To varying degrees it is a feature in all of our devices. It was found to decrease with increasing time between voltage steps, but never disappears fully, and it is still unclear what the source of this hysteresis is, as it is scarcely mentioned in literature. A possible explanation could be the presence of surface traps due to surface modification upon ligand exchange and the presence of dangling bonds. It was found that the hysteresis decreased when the J-V measurement was performed slower, i.e. more time in between voltage steps, and could disappear completely for thin layers. However, slower measurements also resulted in a decreased J_{sc} and are omitted from further discussion. In this study, discussed results are based on the calculation of device characteristics from the J-V curve obtained in backwards direction, as the voltage is decreased from 2 V to -2 V.

3.3.2 IPCE measurements

Although the J-V curve provides insight to many aspects of the device performance, all information gathered from it represents an integrated result from excitations over a wide range of photon energies. To gain insight into the spectral dependence of the device current we measure the external quantum efficiency (EQE), also known as the incident-photon to electron conversion efficiency (IPCE). This is done by measuring the spectral responsivity $S(\lambda)$ of the device over a range of wavelengths and calculating the IPCE using Equation(2.4). We also calculate the expected short circuit current of the

test devices subjected to the AM1.5G spectrum using:

$$J_{sc,calc} = \int_{\lambda_{min}}^{\lambda_{max}} E_R(\lambda) S_T(\lambda) d\lambda \quad (3.2)$$

The device is placed in a portable, airtight sample holder with contact points at the positions of the eight electrodes and transported to a custom-built setup with which the spectral responsivity can be measured. The setup consists of a 50 W quartz tungsten halogen lamp (Newport Research Series), 33 narrow band-pass interference filters (CVI laser) with wavelengths ranging from 400 to 1400 nm, a trans-impedance amplifier and a Stanford research Systems SR830 lock-in amplifier. The setup was calibrated using a Silicon (Newport 818-SL) and a Germanium (Oriol 71653) photodiode. The light from the lamp is monochromatized by the filters and passed through a chopper. Using the chopper in conjunction with a lock-in technique, the response to the monochromatic light can be separated from that of the white background illumination, eliminating the need for a dark environment.

3.3.3 Thickness measurements

After measuring the electrical properties of the device, the thickness of the active layer has to be determined. The device is transported back to the cleanroom where a Veeco Dektak 6M Profilometer is stationed. Using a pincer or a pipet, a scratch is made in the layer of semiconducting material on the glass, in between the ITO and metal areas, while making sure that the glass substrate is reached. The device is then placed beneath the probing tip of the profilometer and a profile scan is made as the probe tip is dragged along the sample, perpendicular to the scratch. Using this profile scan, the layer thickness is obtained by calculating the height difference between the glass substrate and layer top. The Dektak is accurate to ~ 5 nm.

3.3.4 TEM imaging

In order to determine the effect of ligand exchange on inter NC distances, microscopic images are made. This is done using transmission electron microscopy (TEM). TEM is an imaging technique in which an electron beam is passed through a thin film, interacting with the material as it passes through. The electron beam is then magnified, focused and captured by a CCD camera. TEM images are able to reach extremely high resolution, allowing individual PbS NCs to be imaged and even yielding smaller features such as the PbS crystal structure.

3.3.5 Spectroscopy measurements

To perform low-temperature steady state and time-resolved photoluminescence (PL) measurements, samples of o-PbS and PbS-BDT are prepared on quartz substrates. The PbS-BDT samples are fabricated through layer-by-layer spin coating, with intermittent thiol treatments while the o-PbS is deposited by dropcasting. The samples are then loaded into a liquid helium cooled continuous flow (He-flux) Oxford Optistat cryostat. The samples are excited at ~ 380 nm by the second harmonic of a modelocked Ti:Sapphire laser delivering pulses of 150 fs. An optical pulse selector was used to vary the repetition frequency of the exciting pulse. Time-resolved traces were recorded with a Hamamatsu streak camera working in single sweep mode. The steady-state PL spectra in the near-infrared were obtained with an InGaAs detector from Andor and were corrected for the spectral response of the setup. Measurements were performed at temperatures ranging from 5°K to 294°K.

Results

In this chapter the experimental results are presented and discussed. First, the performance of a single layer Schottky device with an active layer consisting of PbS-NCs will be determined. Subsequently, the bilayer device structure will be investigated using active layers consisting of PbS-NC / PCBM and PbS-NC / PCPDTBT. Next, the same materials are investigated in a bulk-heterojunction structure. A novel tandem bulk-heterojunction is also investigated with two stacked bulk-heterojunctions consisting of PbS-NC:PCBM and PbS-NC:PCPDTBT respectively. Next, the performance of a device consisting of a bulk-heterojunction of PCBM:PCPDTBT on top of a layer of PbS-NC is discussed. The effects of ligand exchange will then be investigated by performing TEM and spectroscopy measurements of NC layers before and after ligand exchange.

4.1 Schottky device

As discussed in the theory in Chapter 2, Schottky devices are inherently limited by a number of factors, including: limited exciton dissociation; exciton diffusion to the Schottky contact; the presence of surface recombination states at the metal-semiconductor interface; and a low barrier to hole-injection at the electron collecting contact, allowing recombination and limiting shunt resistance and fill factor. In order to investigate to what degree PbS based devices suffer from these effects, samples were made using PbS NCs as the active layer. A layer-by-layer method was used to deposit the NC films onto the ITO covered substrate. Typically, these films exhibit short range ordering, where each NC is surrounded by the same amount of nearest neighbors (see Figure 4.5a). Intermittent thiol treatments ensured the entire active layer undergoes ligand exchange and the layer-by-layer deposition was repeated until the desired layer thickness was achieved. An annealing step was then performed, placing the substrate on a 140°C hotplate for 10 minutes. The device was finished by thermal evaporation of the top contact consisting

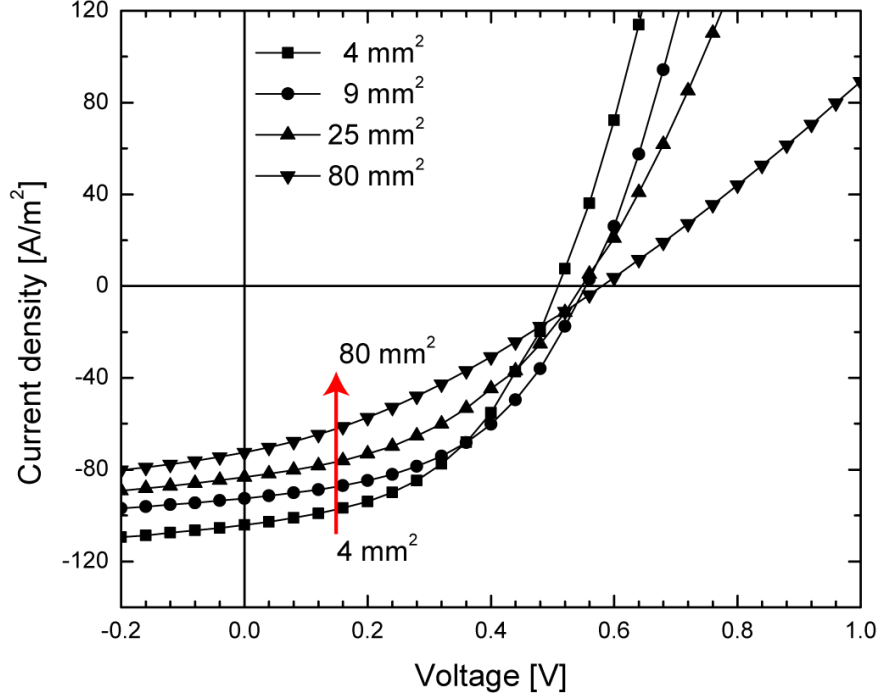


Figure 4.1: J-V curves for the four device areas. With increasing area, the J_{sc} and FF decrease. This typically results in a factor 2 drop of efficiency from area 1 (4 mm^2) to area 4 (80 mm^2).

of 1 nm LiF and 100 nm Al.

Area dependance

In Figure 4.1, the J-V curves are plotted for the four device areas from a single substrate, ranging from 4 mm^2 to 80 mm^2 . It is clear from this figure that device area plays a major role in overall efficiency, with larger device areas performing significantly worse than smaller ones. A decrease is found in both J_{sc} and FF with increasing device area, while the V_{oc} remains roughly constant, resulting in a sharp decrease in efficiency. It was observed throughout this study that the efficiency of the largest cell was typically twice as low as that of the smallest cell. It is as yet unclear what the cause of this phenomenon is. Variable light intensity over the different areas is a possible factor, although it has been found in other studies such as Riedel et al. that light intensity only slightly affects the fill factor, not nearly to degree that we observed, and is therefore unlikely to be the (sole) cause of the area dependence.[14] A more likely effect is that a larger area results in an increased series resistance which leads to lower short circuit current as well as a lower fill factor. Whatever the reason may be, it is clear that it is not possible to make performance comparisons between different sized cells. Therefore, for consistency's sake, only the results of the smallest device areas will be considered throughout the remainder of this chapter.

Batch no.	Excitonic peak [nm]	Thickness [nm]	$V_{oc}[V]$	$J_{oc}[A/m^2]$	$FF[\%]$	$\eta[\%]$
M379	980	~80	0.50	109	46	2.5
M445	1050	~80	0.51	108	53	2.9
M503	1150	~80	0.49	124	59	3.5
M487	1150	~80	0.27	130	26	0.9
M449	1200	~80	0.48	67	46	1.5

Table 4.1: Device characteristics for various batches of PbS NCs

Synthesis dependency

To determine the quality of PbS NCs used, Schottky devices were prepared for each new batch, using the same fabrication procedure as described in Section 3.2. Therefore, the devices differ only in the NCs used, each batch featuring a unique particle size distribution and therefore a different quantum confinement effect and different positions of the first excitonic peak. Table 4.1 shows the performance of several such devices. The difference in performance exhibited is far greater than can be expected by the difference in size (and therefore band gap) alone, indicating that the quality of the nanocrystals is of paramount importance. The quality may be affected by a number of factors, including the age and purity of ingredients used during synthesis, or artifacts in the solvent such as surfactants which have not been fully washed away. Performance comparisons between different device structures are therefore only meaningful within the same batch of PbS nanocrystals.

Thickness dependency

Two Schottky devices, one with a thickness of ~80 nm (15 layers) and one with ~150 nm (25 layers), were prepared from the same batch of NCs according to the layer-by-layer method described in Section 3.2. The results can be found in Figure 4.2. For the 80 nm device an efficiency of 3.53% was obtained, which is exceptional for its relatively small thickness. For the 150 nm device an even higher efficiency of 4.03% was observed, which is among the highest efficiencies recorded in this class of solar cell.[16] Since space charge limited devices are not expected to reach fill factors above 42%,[37] the high fill factors of these devices (59% for the 80 nm device and 57% for the 150 nm device) are an indication that these devices are not space-charge limited, in agreement with the literature, and that the photocurrent is only limited by the generation rate of photoexcitations under illumination.[22, 37] Furthermore, since illumination takes place on the ITO side, i.e. the side of the ohmic contact and not the Schottky barrier, the high fill factors indicate that electrons are capable of electrical field driven transport across the entire 150 nm

distance of the active layer before recombining. This suggests that the active layers of these Schottky devices are fully depleted, as was expected. It also suggests that these devices do not suffer appreciably from a low barrier to hole-injection at the electron collecting contact unlike other Schottky devices. In Figure 4.2b, we see that the 150 nm thick device features a maximum EQE of $\sim 56\%$ throughout the visible and $\sim 11\%$ in the infrared. The EQE of the 80 nm thick device exhibits a similar maximum of $\sim 54\%$, but unlike the thicker device it drops drastically already in the visible, probably due to incomplete absorption of light in that part of the spectrum. Also noteworthy is the much more prominent excitonic-peak of the 150 nm device at 1150 nm, which contributes to the improved performance compared to the thinner device.

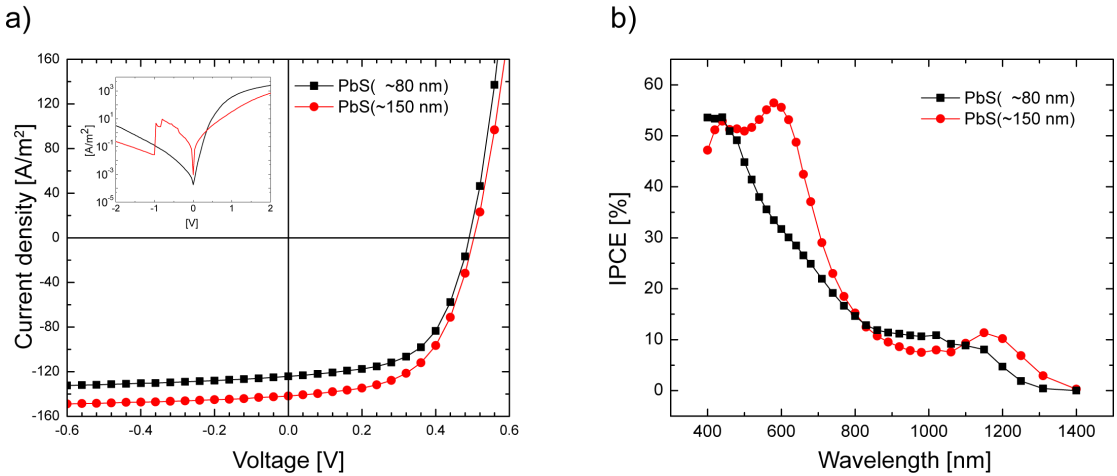


Figure 4.2: (a) J-V curve for PbS-only Schottky device, the J_{sc} of the thicker device (red) is significantly higher leading to an admirable efficiency of 4.0% (b) IPCE spectrum, the thicker device shows a much higher EQE in the visible region as well as a more pronounced excitonic peak at 1150 nm, which accounts for the improved J_{sc}

4.2 Bilayer device

Introducing a heterojunction to facilitate charge separation has been shown to yield improved performance compared to single material Schottky devices. In a recent study of Tsang et al., bilayer devices with a PbS-NC / C60 structure yielded PCEs up to 2.2% compared to 1.6% of a PbS-only device, with the fill factor in particular showing a significant improvement.[38] A similar approach is taken here, using PbS NCs in conjunction with PCBM or PCPDTBT. First, a layer of PbS NCs roughly 80 nm thick was deposited and annealed at 140°C . This was followed by the deposition of the second layer of either PCBM or PCPDTBT from a chloroform solution. The results are shown in Figure 4.3, together with PbS-only devices of the same thickness and same

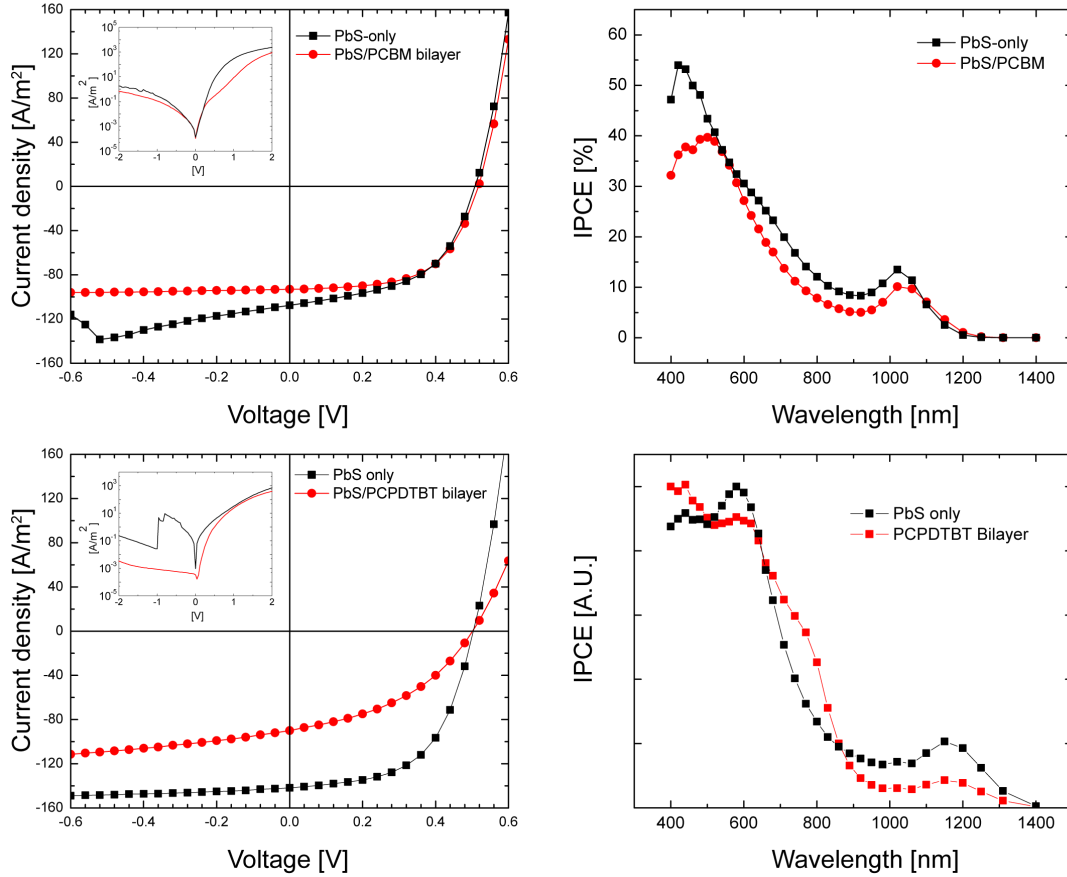


Figure 4.3: (a) PbS/PCBM bilayer (red) shows a diminished J_{sc} but a much improved fill factor. (b) The IPCE of the bilayer is lower than the Schottky device over the whole spectrum, indicating an increase in series resistance. (c) PbS/PCPDTBT (red) yields poor results compared to the Schottky device (black), however the IPCE, (d), does show relatively broader absorption in the visible part of the spectrum. Both IPCE curves have been normalized.

nanocrystal batch. For the PbS-NC/PCBM bilayer device an efficiency of 2.83% was achieved compared to 2.87% for the PbS-only device, a negligible change. Individual parameters do change however. The fill factor is significantly better in the bilayer (59%) than in the Schottky device (53%), which was expected and can be attributed to a more efficient exciton dissociation at the interface between the two materials, and spatially separated transport of the different charge carriers. The effect of this increase is nullified by a decrease in short circuit current which drops from 107.6 to 93.1 A/m². This may be due to an increased series resistance caused by the layer of PCBM. Nevertheless, this device demonstrates that efficient exciton dissociation can occur at the interface between inorganic PbS nanocrystals and organic PCBM molecules. The bilayer of PbS and PCPDTBT performed significantly worse than the PbS-only Schottky device, ex-

hibiting both lower FF and J_{sc} , see Figure 4.3. However, this is most probably caused by an exorbitant thickness of the PCPDTBT layer (120 nm), and it is expected that better efficiencies can be achieved with more tuning of the parameters of the PCPDTBT spin coating program. Measurements of the IPCE of this devices gives further reason for optimism as it shows a broadend IPCE curve, see Figure 4.3d. Specifically, we may expect an improved harvesting of light on the edge of the visible spectrum, where an extra shoulder around 800 nm is observed compared to the curve of the Schottky device.

4.3 Bulk-heterojunction device

The advantages promised by bulk-heterojunction structures have led to increasing interest in such devices within the field of thin-film photovoltaics. Potentially, they offer a solution to the problems of limited exciton diffusion and inefficient dissociation by providing interfaces throughout the active layer at which charge separation may occur. Several device structures employing bulk-heterojunctions were investigated in this study. Firstly, a device was investigated comprising of a layer of PbS-NC and a layer of PCBM, with a blend of the two materials sandwiched in between. First, 8 films of PbS are deposited and individually soaked in 1,4-BDT. Subsequently, a mixture of PbS and PCBM with a weight ratio of 30:1 was spin coated to form a layer of roughly 40 nm. Next, an annealing step was performed at 140°C for 10 minutes, followed by the deposition of a layer of PCBM. Finally the top electrode of LiF and Al is evaporated onto the device, resulting in a device structure of ITO/PbS(40 nm)/PbS:PCBM(40 nm)/PCBM (40 nm)/LiF/Al. This structure yielded an increased efficiency of 3.1% compared to 2.9% from the PbS-only Schottky device, improving the FF from 53% to 57% while the other parameters remained essentially constant. This result is promising because it indicates that the bulk-heterojunction structure may utilize the beneficial characteristics of the bilayer device (i.e. high fill factor) without sacrificing performance of the short circuit current.

Three other active layer structures featuring bulk-heterojunctions were investigated: a simple blend of PbS-NC:PCPDTBT; a device consisting of a layer of PbS-NC with a blend of PCBM:PCPDTBT on top; and a tandem bulk-heterojunction device consisting of a blend of PbS-NC:P3HT topped by a blend of PbS-NC:PCBM. As can be seen in Figures 4.4a-c all three devices structures perform significantly worse than the Schottky structure device made from the same batch of nanocrystals. For the simple PbS-NC:PCPDTBT blend the J_{sc} is significantly lower, decreasing from 88 to 61 A/m² with the V_{oc} and FF remaining roughly constant, resulting in a poor efficiency of 1.9%. The double-blend device also features diminished current characteristics, the J_{sc} dropping

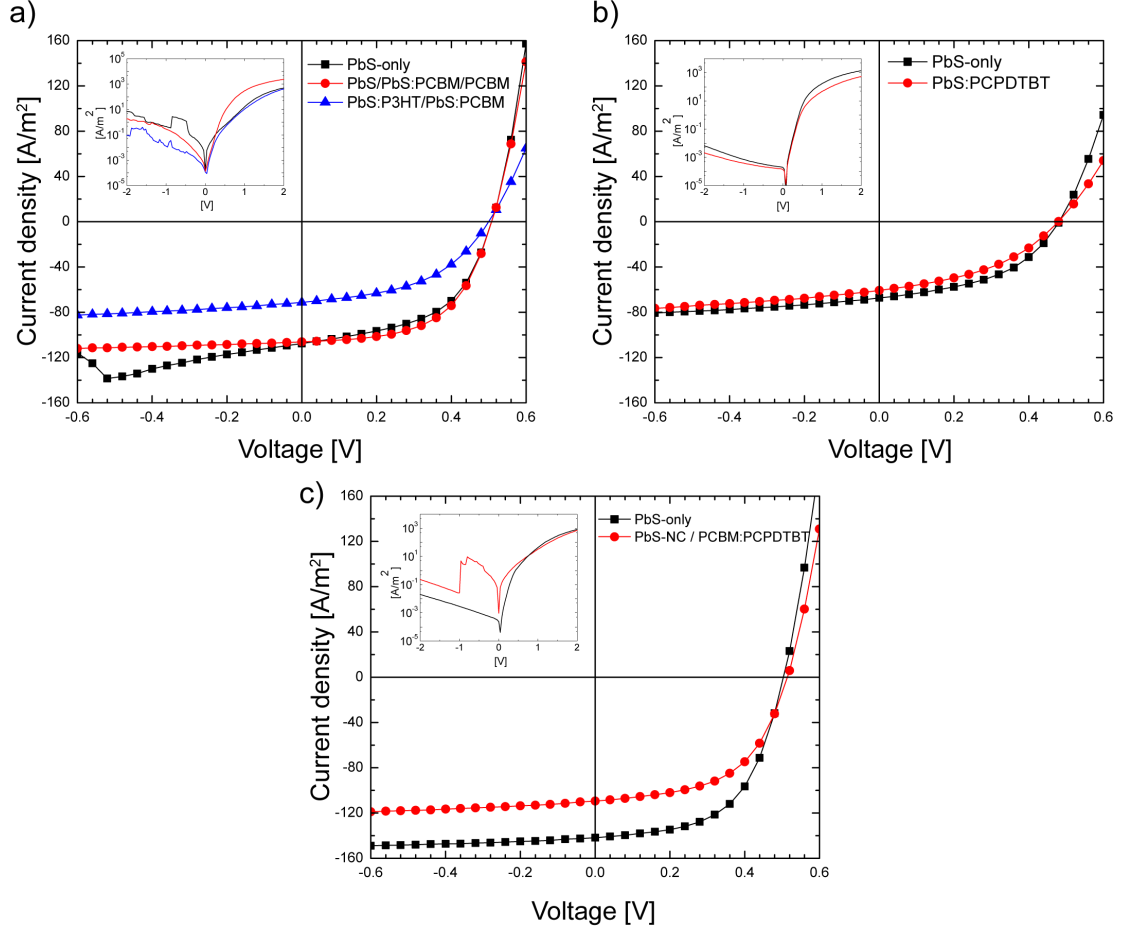


Figure 4.4: Bulk-heterojunction structures with blends of: (a)PbS:PCBM and PbS:P3HT; (b)PbS:PCPDTBT; (c)stacked PbS:P3HT and PbS:PCBM. Only the PbS:PCBM structure shows an improvement with respect to the Schottky device.

significantly from $108 \text{ A}/\text{m}^2$ to $71 \text{ A}/\text{m}^2$ while the V_{oc} and FF also show a slight drop, leading to an efficiency of 1.7%. The device featuring the blend of PCBM:PCPDTBT on top of a layer of PbS features a reasonable efficiency of 3.1%. However, considering that this device was fabricated from high quality NCs and a Schottky device of the same thickness reached 4.0% efficiency, this performance is poor by comparison. Again, it is the J_{sc} that causes the drop in efficiency, decreasing from 142 to $109 \text{ A}/\text{m}^2$, while the FF (54%) and V_{oc} (0.51 V) both slightly increase from 51% and 0.50 V respectively. The increase in FF and V_{oc} indicates that charge separation is indeed occurring more efficiently in the bulk-heterojunction than in the Schottky device. However, we believe that overall performance is limited due to sub-optimal device structure at the nanoscale level, such that percolation pathways do not exist throughout the bulk of the material.

All in all these results demonstrate the difficulties in achieving good morphology of the active layer and the vital importance that it plays in device performance. Because

the device must remain electrically neutral, charge extraction of holes and electrons must take place in equal amounts. The volume ratio of the materials forming the bulk-heterojunction is a crucial parameter in this respect, as well as the resulting morphology at the nanoscale level. If insufficient percolation pathways are available for either the holes or the electrons to reach the electrodes, this will lead to limitation of device performance, particularly in J_{sc} . Nevertheless, it has been demonstrated that charge separation does indeed occur more efficiently than in Schottky type devices, which is very promising. It is our opinion that improvements may be achieved through more investigation in these structures, in particular regarding the optimization of the nanoscale morphology of these devices.

4.4 TEM measurements

A thin film of PbS NCs was dropcast onto two carbon grid substrates from a 2.5 mg/ml solution in chloroform. One substrate was then soaked in a 0.02M solution of 1,4-BDT in acetonitrile for 15 seconds and then carefully dried using a N₂ gun. Both samples were studied using transmission electron microscopy in order to determine the effect of ligand exchange on the inter-NC separation distance. Comparing the NCs before ligand exchange (Figure 4.5a) and after (Figure 4.5b) confirms the hypothesis that exchanging oleic acid ligands with the shorter 1,4-BDT molecules significantly decreases the particle spacing. The average spacing between particles can be estimated to be ~ 2 nm before ligand exchange and ~ 0.5 nm afterwards, which is in good agreement with the study performed by Choi et al., in which respective values of 1.8 nm and 0.5 nm were found.[39] The separation reduction is non-homogeneous, indicating a large variance in the degree of crosslinking throughout the layer. It is probable that a significant percentage of thiols bind to the surface of the same nanocrystal, while others bind to nearby particles. In a study by Talapin et al. it was shown that decreasing the inter-NC spacing increases the conductivity of NC layers dramatically, by as much as ~ 10 orders of magnitude.[40] Therefore it can be safely stated that charge transport is greatly enhanced by thiol treatment of the NC film.

4.5 Optical properties of PbS NCs

In this section the optical properties of thin PbS NC films are investigated. To obtain a better understanding of the working mechanisms of PbS devices and the physics of the crosslinked NC arrays, it is interesting to investigate their optical properties and in particular the temperature dependence thereof. Such measurements have been performed

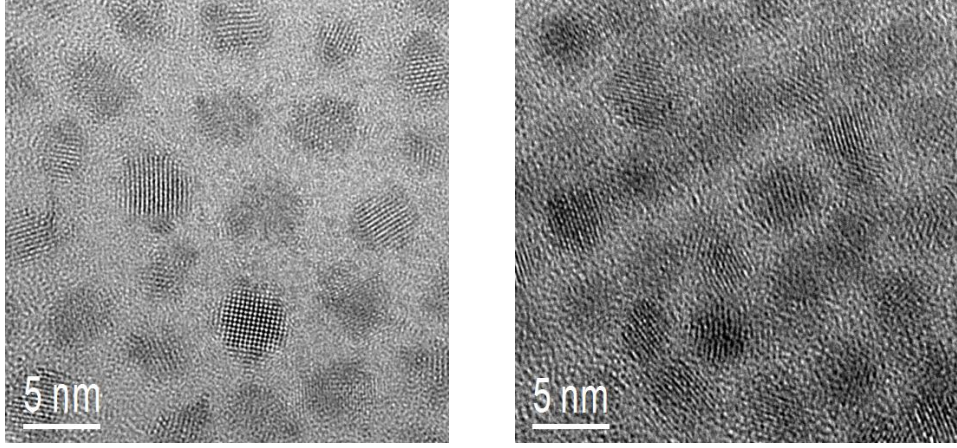


Figure 4.5: PbS NCs (a) before and (b) after exposure to 1,4-BDT

with PbS NCs capped with insulating organic ligands,[41, 42] but have not been done before on post deposition ligand-exchanged films of PbS NCs. Samples of o-PbS and of thiol treated PbS-BDT thin films were prepared (see Section 3.3.5) and steady state PL measurements were performed at temperatures varying from room temperature to 5°K. In Figure 4.6a the steady state PL spectra of the o-PbS film are displayed for various temperatures. It is evident that the PL spectra are very much temperature dependent. At room temperature, the PL of o-PbS shows a maximum at 1242 nm, which undergoes a significant red-shift with decreasing temperature, resulting in a maximum at 1346 nm at 5°K. Furthermore, the full width at half maximum (FWHM) of the PL peak at 5°K is decreased to 46% of its value at room temperature. In addition to this, the PL intensity increases by more than a factor of four with decreasing temperature. The red shift can be explained by thermal expansion of the band gap of PbS. As the temperature changes, the lattice constant (i.e. the distance between neighboring Pb positions) is altered, as well as the amount of electron-phonon interactions. This gives rise to the band gap temperature coefficient dE_g/dT , which is positive for PbS NCs in this size range. This leads to a decreasing band gap for lower temperatures and to the shift in the maximum of the PL spectra to smaller wavelengths. The decrease of the FWHM and the increase of the PL intensity can be attributed to the lower density of phonons at lower temperatures and resulting in a lower probability of phonon-coupled quenching of excitons. This temperature-induced red shift and narrowing of the PL spectra is consistent with previously reported results by Lui et al.[43]

When the surface of the o-PbS NCs is modified by exposure to BDT molecules the spectra become more complicated and show peculiar characteristics. At room temperature the PL spectra of PbS-BDT is shifted towards the red with respect to the o-PbS spectra as illustrated by Figure 4.6c. This red-shift can be attributed to the change in the

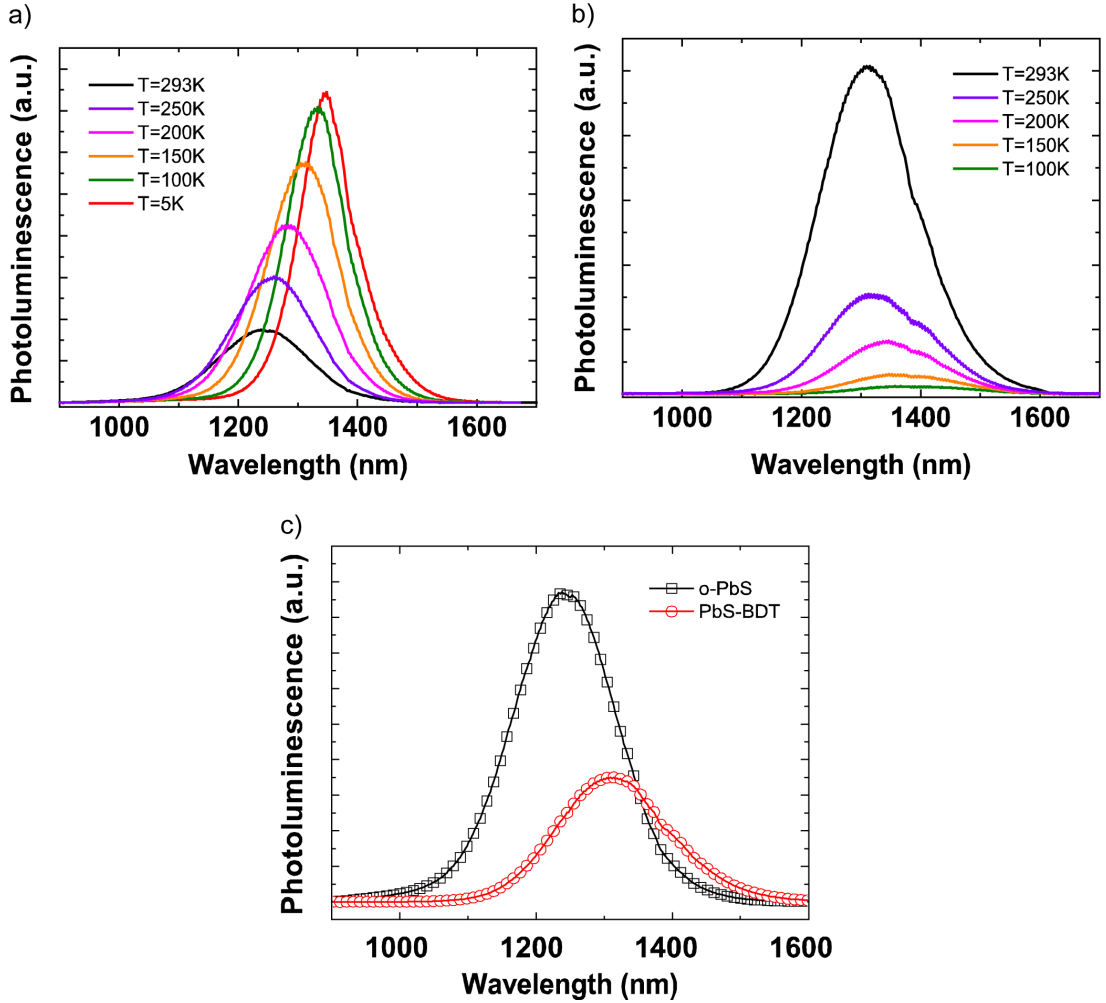


Figure 4.6: Steady-state PL spectra of (a) o-PbS NCs and (b) PbS-BDT at different temperatures. (c) Comparison of the steady-state PL spectra of the o-PbS NCs and PbS-BDT at 293°K.

average dielectric constant of the layer that occurs with ligand exchange. An additional red shift is observed (Figure 4.6b) similar to what occurs with the o-PbS for decreasing temperatures, due to the same thermal expansion effect as before. However, in contrast to the increased intensity found with o-PbS, decreasing temperature was observed to cause a decreasing PL intensity instead, along with a broadening of the peaks. This is counter intuitive, as one would expect that the decreased influence of phonon-electron interactions would lead to a higher intensity at lower temperatures. Similar results found by Wuister et al. with CdTe quantum dots suggest that surface passivation decreases with temperature due to a phase transition of the ligands and displacement of the surface atoms, which results in a decrease in non-radiative relaxation rates with temperature.[44] Therefore capping ligands play a role not only in stabilization of the NC and confinement of the charge carriers, but also in the passivation of dangling bonds on the NC

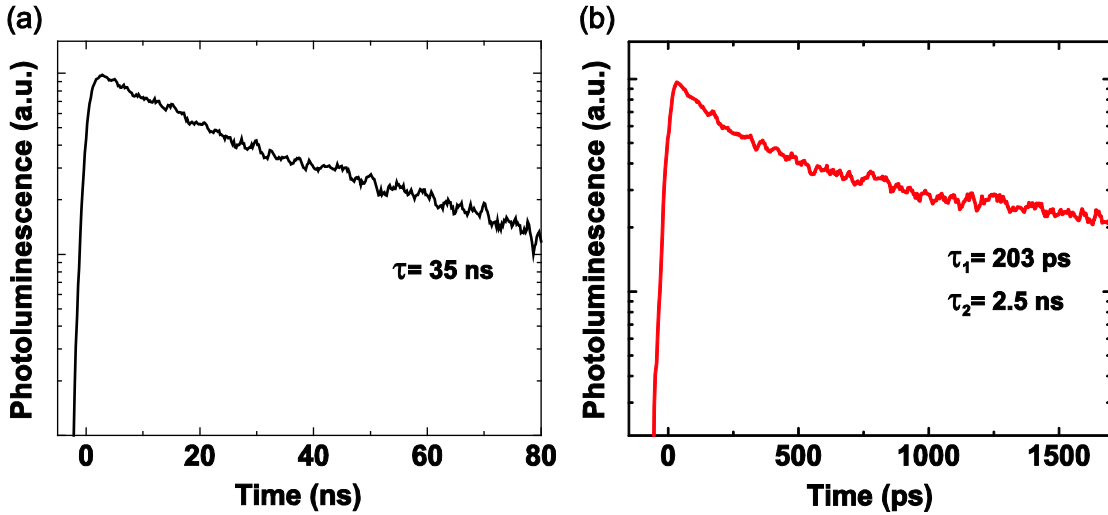


Figure 4.7: PL decay of (a) o-PbS and (b) PbS-BDT at 293°K.

surface. Because surface passivation is an important factor in the prevention of exciton recombination sites, the type of capping ligand used can play a significant role in device performance.

In addition to steady state PL measurements, time resolved measurements were performed at room temperature on samples of o-PbS and samples of thiol treated PbS-BDT. The PL decay of PbS before and after treatment are shown in Figure 4.7. With oleic acid ligands, the PL of PbS shows a monoexponential decay with a decay constant of ~ 35 ns. After surface treatment with BDT, this behavior instead becomes a bi-exponential decay with a component of ~ 2.5 ns and one of ~ 203 ps. We ascribe the bi-exponential behavior and shorter lifetime to: i) depopulation of the excitonic level and transfer to the defect states and ii) partial relaxation of the quantum confinement due to the decrease in inter-particle separation after the thiol treatment.

Conclusions

In this study the use of PbS nanocrystal material as a component in efficient but easily processable photovoltaic devices is explored. Schottky type devices based on PbS NCs are demonstrated to achieve excellent efficiencies of up to 4.0% in combination with exceptionally high fill factors of up to 59%. The quality of the NCs used is found to be of crucial importance in determining device performance.

PbS NC based bilayer devices are fabricated, most successfully in combination with PCBM, improving V_{oc} from 0.51 V to 0.52 V and FF from 53% to 59% compared with a PbS-only Schottky device of the same thickness, but simultaneously suffering a drop in J_{sc} resulting in a negligible change in overall efficiency. Nevertheless, the high fill factor indicates efficient exciton dissociation takes place at the PbS - PCBM interface.

Several novel device structures incorporating bulk-heterojunctions are investigated. A device comprising of a layer of PbS, a blend of PbS-PCBM, and a layer of PCBM exhibits improved performance compared to a Schottky device, increasing the fill factor from 53% to 57% without significantly affecting the V_{oc} or J_{sc} , thus increasing efficiency from 2.9% to 3.1%. Three other device structures incorporating bulk-heterojunctions are investigated. A blend of PbS and PCPDTBT yields an efficiency of 1.9%, a tandem bulk-heterojunction device with structure PbS:P3HT/PbS:PCBM yields 1.7% while an active-layer structure of PbS/PCBM:PCPDTBT yields an efficiency of 3.1%. In all three cases the efficiency is lower than the referential Schottky devices and in each case it is primarily caused by a drop in J_{sc} . We attribute this to a sub-optimal morphology at the nanoscale level such that insufficient percolation pathways are formed. Improvements may be expected with additional tweaking of the fabrication procedure.

TEM images of NC films made before and after ligand exchange show that inter particle spacing is decreased from ~ 2 nm with long oleic acid ligands to ~ 0.5 nm after treatment with 1,4-BDT. After treatment the variation in spacing increases due to non-homogeneous crosslinking of the individual nanocrystals.

The PL spectra of PbS before and after ligand exchange are investigated and found to be heavily temperature dependent. The PL spectra of both o-PbS and PbS-BDT undergo a redshift with decreasing temperature, which is caused by the positive thermal coefficient of the band gap for PbS nanocrystals. An additional redshift occurs when the long oleic acid ligands are replaced by shorter 1,4-BDT molecules, due to a change in average dielectric constant of the PbS film. The intensity and FWHM of the PL peaks show contrasting temperature dependencies before and after thiol treatment. For o-PbS at 5°K, the PL spectra exhibit more than 4 times higher intensity and a FWHM of 46% compared with room temperature. PbS-BDT shows the opposite behavior, exhibiting decreasing intensity and broadening peaks as the temperature is decreased, indicating wave function overlap and an increase of non-radiative pathways at lower temperatures caused by exciton-trapping defect states on the nanocrystal surface. The radical change in optical properties upon ligand exchange demonstrates the importance of proper ligand selection in achieving good device performance.

All in all, the excellent performance of PbS NCs demonstrated in Schottky type devices, in conjunction with their adaptability in both band gap and surface properties make them a promising material in the search for high efficiency, but easily processable photovoltaics.

References

- [1] J. Chow, R. J. Kopp, and P. R. Portney, “Energy Resources and Global Development,” *Science*, vol. 302, p. 1528, 2003.
- [2] K. Knapp and T. Jester, “Empirical Investigation of the Energy Payback Time for Photovoltaic Modules,” *Solar Energy*, vol. 71, no. 3, pp. 165–172, 2001.
- [3] A. Einstein, “On a Heuristic Viewpoint Concerning the Production and Transformation of Light,” *Annalen der Physik*, vol. 17, no. 13, pp. 132–148, 1905.
- [4] M. A. Green, K. Emery, Y. Hishikawa, and W. Warta, “Solar Cell Efficiency Tables,” *Prog. Photovolt: Res. Appl.*, vol. 19, pp. 84–92, 2011.
- [5] T. Rauch, M. Böberl, S. F. Tedde, J. Fürst, M. V. Kovalenko, G. Hesser, U. Lemmer, W. Heiss, and O. Hayden, “Near-Infrared Imaging with Quantum-Dot Sensitized Organic Photodiodes,” *Nature Photonics*, vol. 3, p. 332, 2009.
- [6] X. Jiang, R. D. Schaller, S. B. Lee, J. M. Pietryga, V. I. Klimov, and A. A. Zakhidov, “PbSe Nanocrystal/Conducting Polymer Solar Cells With an Infrared Response to 2 Micron,” *J. Mater. Res.*, vol. 22, no. 8, pp. 2204–2210, 2007.
- [7] C. W. Tang, S. A. VanSlyke, and C. H. Chen, “Electroluminescence of Doped Organic Thin Films,” *J. Appl. Phys.*, vol. 65, no. 9, pp. 3610–3616, 1989.
- [8] W. Shockley and H. Queisser, “Detailed Balance of Efficiency of p-n Junction Solar Cells,” *J. Appl. Phys.*, vol. 32, no. 3, pp. 510–519, 1961.
- [9] V. Coropceanu, J. Cornil, D. A. da Silva Filho, Y. Olivier, R. Silbey, and J. Brédas, “Charge Transport in Organic Semiconductors,” *Chem. Rev.*, vol. 107, p. 930, 2007.
- [10] T. Sameshima, K. Saitoh, M. Sato, A. Tajima, and N. Takashima, “Crystalline Properties of Laser Crystallized Silicon Films,” *Jpn. Jnl. Appl. Phys.*, vol. 36, p. 1361, 1997.
- [11] H. Hoppe and N. S. Sariciftci, “Crystalline Properties of Laser Crystallized Silicon Films,” *J. Mater. Res.*, vol. 19, no. 7, p. 1924, 2004.

- [12] B. A. Gregg and M. C. Hannai, "Comparing Organic to Inorganic Photovoltaic Cells: Theory, Experiment, and Simulation," *J. Appl. Phys.*, vol. 93, no. 6, p. 3606, 2003.
- [13] D. V. Talapin, J. S. Lee, M. V. Kovalenko, and E. V. Shevchenko, "Prospects of Colloidal Nanocrystals for Electronic and Optoelectronic Applications," *Chem. Rev.*, vol. 110, no. 1, p. 428, 2010.
- [14] I. Riedel, J. Parisi, V. Dyakonov, L. Lutsen, D. Vanderzande, and J. C. Hummelen, "Effect of Temp and Illumination on Electrical Characteristics of Polymer-Fullerene Bulk-Heterojunction Solar Cells," *Adv. Funct. Mater.*, vol. 15, no. 1, pp. 58–61, 2004.
- [15] B. P. Rand and D. P. Burk, "Offset Energies at Organic Semiconductor Heterojunctions and their Influence on the Open-Circuit Voltage of Thin-Film Solar Cells," *Phys. Rev. B*, vol. 75, pp. 115327–1, 2007.
- [16] J. Tang and E. H. Sargent, "Infrared Colloidal Quantum Dots for Photovoltaics: Fundamentals and Recent Progress," *Adv. Mater.*, vol. 23, no. 1, pp. 12–29, 2011.
- [17] J. M. Luther, M. Law, M. C. Beard, Q. Song, M. O. Reese, R. J. Ellingson, and A. J. Nozik, "Schottky Solar Cells Based on Colloidal Nanocrystal Films," *Nano Lett.*, vol. 8, no. 10, pp. 3488–3492, 2008.
- [18] A. G. Pattantyus-Abraham, I. J. Kramer, A. R. Barkhouse, X. Wang, G. Konstantatos, R. Debnath, L. Levina, I. Raabe, M. Nazeeruddin, M. Graÿltzel, and E. H. Sargent, "Depleted-Heterojunction Colloidal Quantum Dot Solar Cells," *ACS Nano*, vol. 4, no. 6, pp. 3374–3380, 2010.
- [19] R. Debnath, J. Tang, D. A. Barkhouse, X. Wang, A. G. Pattantyus-Abraham, L. Brzozowski, L. Levina, and E. H. Sargent, "Ambient-Processed Colloidal Quantum Dot Solar Cells via Individual Pre-Encapsulation of Nanoparticles," *J. Am. Chem. Soc.*, vol. 132, no. 7, pp. 5952–5953, 2010.
- [20] N. S. Sariciftci, L. Smilowitz, A. J. Heeger, and F. Wudi, "Photoinduced Electron Transfer from a Conducting Polymer to Buckminsterfullerene," *Science*, vol. 258, p. 1474, 1992.
- [21] J. M. Luther, J. Gao, M. T. Lloyd, O. E. Semonin, M. C. Beard, and A. J. Nozik, "Stability Assessment on a 3% Bilayer PbS/ZnO Quantum Dot Heterojunction Solar Cell," *Adv. Mater.*, vol. 22, p. 3704, 2010.

- [22] J. Tang, L. Brzozowski, D. A. R. Barkhouse, X. Wang, R. Debnath, R. Wolowiec, E. Palmiano, L. Levina, A. G. Pattantyus-Abraham, D. Jamakosmanovic, E. H. Sargent, M. C. Beard, and A. J. Nozik, "Quantum Dot Photovoltaics in the Extreme Quantum Confinement Regime: The Surface-Chemical Origins of Exceptional Air- and Light-Stability," *ACS Nano*, vol. 4, no. 2, pp. 869–878, 2010.
- [23] S. A. McDonald, G. Konstantatos, S. Zhang, P. W. Cyr, E. J. D. Klem, L. Levina, and E. H. Sargent, "Solution-Processed PbS Quantum Dot Infrared Photodetectors and Photovoltaics," *Nature Materials*, vol. 4, pp. 138 – 142, 2005.
- [24] K. Szendrei, *Charge Extraction from Colloidal Inorganic Nanocrystals*. PhD thesis, University of Groningen, 2011.
- [25] E. J. D. Klem, H. Shukla, S. Hinds, D. D. MacNeil, L. Levina, and E. H. Sargent, "Impact of Dithiol Treatment and Air Annealing on the Conductivity, Mobility, and Hole Density in PbS Colloidal Quantum Dot Solids," *Appl. Phys. Lett.*, vol. 92, p. 212105, 2008.
- [26] D. A. R. Barkhouse, A. G. Pattantyus-Abraham, L. Levina, and E. H. Sargent, "Thiols Passivate Recombination Centers in Colloidal Quantum Dots Leading to Enhanced Photovoltaic Device Efficiency," *ACS Nano*, vol. 2, no. 11, pp. 2356–2362, 2008.
- [27] K. Sugiyama, H. Ishii, Y. Ouchi, and K. Seki, "Dependence of Indium-Tin-Oxide Work Function on Surface Cleaning Method as Studied by Ultraviolet and X-ray Photoemission Spectroscopies," *J. Appl. Phys.*, vol. 87, no. 1, pp. 295–298, 2008.
- [28] M. A. Hines and G. D. Scholes, "Colloidal PbS Nanocrystals with Size-Tunable Near-Infrared Emission: Observation of Post-Synthesis Self-Narrowing of the Particle Size Distribution," *Adv. Mater.*, vol. 15, no. 21, pp. 1844–1849, 2003.
- [29] L. J. A. Koster, V. D. Mihailetschi, and P. W. M. Blom, "Ultimate Efficiency of Polymer/Fullerene Bulk Heterojunction Solar Cells," *Appl. Phys. Lett.*, vol. 88, no. 9, pp. 093511–1, 2006.
- [30] M. Reyes-Reyes, K. Kim, and D. L. Carroll, "High-Efficiency Photovoltaic Devices Based on Annealed Poly(3-Hexylthiophene) and 1-(3-Methoxycarbonyl)-Propyl-1-Phenyl-(6,6)C61 Blends," *Appl. Phys. Lett.*, vol. 87, no. 8, pp. 083506–1, 2005.
- [31] M. Morana, M. Wegscheider, A. Bonanni, N. Kopidakis, S. Shaheen, M. Scharber, Z. Zhu, D. Waller, R. Gaudiana, and C. Brabec, "Bipolar Charge Transport

- in PCPDTBT-PCBM Bulk-Heterojunctions for Photovoltaic Applications,” *Adv. Funct. Mater.*, vol. 18, no. 12, pp. 1757–1766, 2008.
- [32] J. Y. Kim, K. Lee, N. E. Coates, D. Moses, T. Nguyen, M. Dante, and A. J. Heeger, “Efficient Tandem Polymer Solar Cells Fabricated by All-Solution Processing,” *Science*, vol. 317, no. 5835, pp. 222–225, 2007.
- [33] D. Mühlbacher, M. Scharber, M. Morana, Z. Zhu, D. Waller, R. Gaudiana, and C. Brabec, “High Photovoltaic Performance of a Low-Bandgap Polymer,” *Adv. Mater*, vol. 18, no. 21, pp. 2884–2889, 2006.
- [34] J. Tang, X. Wang, L. Brzozowski, D. A. R. Barkhouse, R. Debnath, L. Levina, and E. H. Sargent, “Schottky Quantum Dot Solar Cell Stable in Air Under Solar Illumination,” *Adv. Mater*, vol. 22, no. 12, pp. 1398–1402, 2010.
- [35] Y. Kim, S. A. Choulis, J. Nelson, D. D. C. Bradley, S. Cook, and J. R. Durrant, “Device Annealing Effect in Organic Solar Cells with Blends of Regioregular Poly(3-Hexylthiophene) and Soluble Fullerene,” *Adv. Mater*, vol. 86, no. 6, pp. 063502 – 063502–3, 2009.
- [36] W. Gomulya Master’s thesis, University of Groningen, 2011.
- [37] K. Szendrei, *Charge Extraction from Colloidal Inorganic Nanocrystals*. PhD thesis, University of Groningen, 2011.
- [38] S. W. Tsang, H. Fu, R. Wang, J. Lu, K. Yu, and Y. Tao, “Highly Efficient Cross-linked PbS Nanocrystal/C60 Hybrid Heterojunction Photovoltaic Cells,” *Appl. Phys. Lett*, vol. 95, no. 18, pp. 183505–1–183505–3, 2009.
- [39] J. J. Choi, J. Luria, B. R. Hyun, A. C. Bartnik, L. Sun, Y. F. Lim, J. A. Marohn, F. W. Wise, and T. Hanrath, “Photogenerated Exciton Dissociation in Highly Coupled Leadsalt Nanocrystal Assemblies,” *Nano Lett.*, vol. 10, no. 5, pp. 1805–1811, 2010.
- [40] D. V. Talapin and C. B. Murray, “PbSe Nanocrystal Solids for n- and p-Channel Thin Film Field-Effect Transistors,” *Science*, vol. 310, no. 5745, pp. 86–89, 2005.
- [41] A. Olkhovets, R. C. Hsu, A. Lipovskii, and F. W. Wise, “Size-Dependent Temperature Variation of the Energy Gap in Lead-Salt Quantum Dots,” *Phys. Rev. Lett.*, vol. 81, no. 16, pp. 3539–3542, 1988.
- [42] D. Kim, T. Kuwabara, and M. J. Nakayama, “Photoluminescence Properties Related to Localized States in Colloidal PbS Quantum Dots,” *J. Lumin*, vol. 119, pp. 214–218, 2006.

-
- [43] C. Liu, Y. K. Kwon, and J. Heo, "Absorption and Photoluminescence of PbS QDs in Glasses," *J. Non-Cryst. Solids*, vol. 355, no. 37, pp. 1880–1883, 2006.
- [44] S. F. Wuister, A. van Houselt, C. de Mello Donegá, D. Vanmaekelbergh, and A. Meijerink, "Temperature Antiquenching of the Luminescence from Capped CdSe Quantum Dots," *Angew. Chem. Int. Ed.*, vol. 116, no. 23, pp. 3091–3095, 2004.